

Simulation, Fabrication and Characterization of Photonic Crystals

Michael Adler

Technische Universität Berlin

Fakultät II: Mathematik und Naturwissenschaften
Institut für theoretische Physik



A thesis submitted to the Technische Universität Berlin
for the degree of Master of Science in Physics

Eidesstattliche Erklärung

Die selbständige und eigenhändige Anfertigung versichert an Eides statt

Berlin, den 9. Mai 2013

Michael Adler

Simulation, Fabrication and Characterization of Photonic Crystals

Michael Adler

Photonische Kristalle (PK) gehören zu den Metamaterialien, die auch natürlich vorkommen. Fortgeschrittene numerische Werkzeuge und moderne Nanofabrikationsverfahren erlauben Simulation und Herstellung photonischer Kristalle für verschiedenste Anwendungen.

Im Mittelpunkt der vorliegenden Arbeit steht die Simulation, die anschließende Fabrikation und optische Charakterisierung von freistehenden photonischen Kristallresonatoren (L3) für den sichtbaren Wellenlängenbereich. Ferner wird noch ein Resonator, der auf der lokalen Breitenmodifikation eines linearen Defekts basiert, vorgestellt. Als Substrat wird stöchiometrisches Siliziumnitrid (Si_3N_4) verwendet. Die photonischen Kristalle werden hinsichtlich des Gütefaktors (Q) optimiert, es kommen Finite-Differenzen-Methoden (FDTD) zur Anwendung. Die Simulationen ergeben nur moderate Q -Faktoren für die L3-Kavitäten. Gleichwohl werden hohe Q -Faktoren (700.000) für die andere Struktur errechnet.

Elektronenstrahl-Lithographie sowie physikalische und chemische Ätzverfahren werden zur Fabrikation verwendet. Die so hergestellten Proben werden mittels Fluoreszenzspektroskopie basierend auf der intrinsischen Fluoreszenz von Si_3N_4 charakterisiert. Hierbei fällt ein Unterschied zwischen theoretischen und experimentell ermittelten Q -Faktoren auf. Eine Diskrepanz ergibt sich auch für die theoretischen und die experimentellen Resonanzwellenlängen. Lochradius sowie Si_3N_4 -Schichtdicke sind nicht genau bekannt. Dies ist wahrscheinlich die Hauptursache für die beobachteten Diskrepanzen. Für weitergehende quantitative Vergleiche

zwischen Theorie und Simulation ist daher eine weitere Optimierung des Herstellungsprozesses erforderlich.

“My parents”

Contents

Abbreviations	1
Introduction	3
1 Photonic Crystal Theory	5
1.1 Photonic crystal properties	5
1.1.1 Maxwell's equations	5
1.1.2 Analogies from solid state physics	9
1.1.3 Planar photonic crystals	15
1.1.4 Resonant cavity parameters	19
1.2 The nitrogen vacancy center of diamond	22
1.3 Numerical methods	22
1.3.1 General overview of different methods	24
1.3.2 The plane wave expansion method	24
1.3.3 Finite differences	25
1.3.4 The finite-difference time-domain method	26
1.3.5 The finite-difference frequency-domain method	29
2 Photonic Crystal Simulations	31
2.1 Finite-difference frequency-domain simulations	32
2.1.1 The influence of the resolution	32
2.1.2 Results of band structure simulations	33
2.2 Finite-difference time-domain simulations	36
2.2.1 Optimization and investigation of $L3$ cavities	37
2.2.2 Cavity realized by local width modulation of a line defect	46
3 Fabrication and Characterization	49
3.1 Fabrication of photonic crystal cavities	49
3.1.1 Pattern generation	50

3.1.2	Pattern transfer	51
3.2	Characterization of photonic crystals	52
3.3	Experimental results	52
3.3.1	Fabrication	54
3.3.2	Measurements	55
4	Summary and Outlook	59
4.1	Summary	59
4.1.1	Simulations	59
4.1.2	Fabrication and characterization	60
4.2	Conclusion and outlook	60
	Acknowledgments	63
	Bibliography	65
	Publications	69
	List of Figures	71
	List of Tables	75

Abbreviations

a.u.	arbitrary units
BS	beam splitter
BZ	Brillouin zone
ca.	circa
CCD	charge-coupled device
CW	continuous wave
e.g.	<i>exempli gratia</i> (for instance)
EBL	electron beam lithography
et al.	<i>et alii</i> (and others)
etc.	<i>et cetera</i> (and so forth)
FDFD	finite-difference frequency-domain
FDTD	finite-difference time-domain
FFT	fast Fourier transform
FM	flip mirror
FWHM	full-width half-maximum
HZB	Helmholtz-Zentrum Berlin für Materialien und Energie GmbH
i.e.	<i>id est</i> (that is)
LASER	light amplification by stimulated emission of radiation
LED	light-emitting diode
LPCVD	low-pressure chemical vapor deposition
NA	numerical aperture
No.	<i>numero</i> (number)
NV	nitrogen vacancy

PBG	photonic band gap
PC	photonic crystal
PDE	partial differential equation
PML	perfectly matched layer
PMMA	polymethylmethacrylate
QED	quantum electrodynamics
QIP	quantum information processing
RIE	reactive ion etching
SEM	scanning electron microscope
SPEC	spectrograph
TE	transverse electric
TIR	total internal reflection
TM	transverse magnetic
ZPL	zero phonon line

Introduction

The sophisticated machinery of modern nanotechnology [1] is required to fabricate *photonic crystals*. Yet, Magnificent three-dimensional crystals are found in the domain of nature. Its representants are well-known. The Rhetenor Blue Morpho (*Morpho rhetenor*) butterfly's wing scale, see Figure 0.1, is an example for natural photonic crystals [2]. In fact, many other examples exist [3].

It is the periodic change of the dielectric constant that lies behind the above-mentioned colorful effects [4]. As the basic physical effect rests upon diffraction, the periodicity of the photonic crystal structure has to be in the length-scale of the electromagnetic waves. The fundamental optical properties of photonic crystals are easily understood with MAXWELL's *equations* [5]. Even though photonic crystals are known since 1887 [6], it was not until 1987 when YABLONOVITCH *et al.* published their seminal paper on photonic crystal properties, especially on the possibility of a two- and three-dimensional photonic band gap, that the subject matter became popular [7, 8]. It took another 13 years, and a silicon photonic crystal with a complete three-dimensional photonic band gap was produced [9]. Among the necessary tools for photonic crystals are modern nanofabrication technologies [1] as well as simulation tools [10–12]. Nowadays, photonic



Figure 0.1: Rhetenor Blue Morpho. Its uniform color and reflectivity can be explained by a photonic crystal model. From [2].

crystals have become a hot topic with a plethora of different applications, a lot of basic research still lies ahead of us.

The thesis is structured as follows. The first chapter offers a glimpse into the theory of photonic crystals, and into the numerical methods required to simulate photonic crystal properties. Based on prior research, simulations of photonic crystals are conducted using the work reported in [10, 11]. Selected results are presented in the second chapter. Finally, photonic crystal samples are produced. The theory of fabrication and characterization of the samples is outlined in the first part of the chapter. The second part is devoted to the experimental results and their interpretation. The thesis finishes with a summary and a conclusion.

Chapter 1

Photonic Crystal Theory

In this chapter we shall review the basic physics required to understand photonic crystals. The presentation is inspired by [13] where a more complete survey of the topic can be found. An advanced view on photonic crystals has been taken by [14]. Additionally, concepts from solid state physics crystals [15] will be motivated, where relevant. At the end, numerical methods that are commonly used to simulate photonic crystal structures are briefly introduced.

1.1 Photonic crystal properties

1.1.1 Maxwell's equations

We will first review Maxwell's equations [16] so as to understand the propagation of light in a photonic crystal. For the sake of simplicity, a linear and lossless dielectric will be considered. This causes some loss of generality [13].

The electromagnetic (and by the same token also optic) properties of a photonic crystal are governed by Maxwell's equations. In the absence of charge ρ and currents \mathbf{j}

Maxwell's equations read [17]:

$$\nabla \cdot \mathbf{D} = 0, \quad (1.1)$$

$$\nabla \times \mathbf{E} = -\frac{\partial \mathbf{B}}{\partial t}, \quad (1.2)$$

$$\nabla \cdot \mathbf{B} = 0, \quad (1.3)$$

$$\nabla \times \mathbf{H} = \frac{\partial \mathbf{D}}{\partial t}, \quad (1.4)$$

where \mathbf{E} and \mathbf{H} are the macroscopic electric and magnetic fields. Electric displacement field and magnetic field are denoted by \mathbf{D} and \mathbf{B} . The next step is to express Maxwell's equations in terms of macroscopic fields.

Fortunately, it is possible to find a relation between \mathbf{E} and \mathbf{D} and between \mathbf{B} and \mathbf{H} [17]. This helpful, though idealized relation is called *constitutive relation*. The relation is based on the quite general assumption that the components D_i of \mathbf{D} are related to E_i of \mathbf{E} via a power series [13]:

$$D_i/\varepsilon_0 = \sum_i \varepsilon_{ij} E_j + \sum_{jk} \chi_{ijk} E_j E_k + \mathcal{O}(E^3), \quad (1.5)$$

where ε_0 , the *permittivity of free space*, is $= (\mu_0 c_0^2)^{-1} \approx 8.854 \times 10^{-12} \text{ Fm}^{-1}$. \mathbf{B} and \mathbf{H} are connected through

$$\mathbf{B} = \mu_0 \mathbf{H}. \quad (1.6)$$

The eigenvalue problem

Maxwell's equations can be further simplified. This approximation is reasonable for many dielectric materials [13]. As pointed out there, four assumptions are necessary for the approximation.

1. Small field strengths, i.e. linear regime of χ .
2. Macroscopic and isotropic material: $\mathbf{D}(\mathbf{r}, \omega) \propto \mathbf{E}(\mathbf{r}, \omega) \cdot \varepsilon(\mathbf{r}, \omega)$.
3. Non-dispersive material, i.e. $\frac{\partial \varepsilon}{\partial \omega} = 0$.
4. Transparent materials, i.e. $\varepsilon \in \mathbb{R}^+$.

Following [13], it will be assumed that the magnetic permeability is close to unity. Using the above-mentioned assumptions yields the constitutive relations for linear, non-dispersive and isotropic media:

$$\mathbf{D}(\mathbf{r}, t) = \varepsilon_0 \varepsilon(\mathbf{r}) \mathbf{E}(\mathbf{r}, t), \quad (1.7)$$

$$\mathbf{H}(\mathbf{r}, t) = \frac{1}{\mu_0} \mathbf{B}(\mathbf{r}, t). \quad (1.8)$$

Based on (1.8) and (1.7), Maxwell's equations can be recast into the following form

$$\nabla \cdot \mathbf{H}(\mathbf{r}, t) = 0, \quad (1.9)$$

$$\nabla \times \mathbf{E}(\mathbf{r}, t) + \mu_0 \frac{\partial \mathbf{H}(\mathbf{r}, t)}{\partial t} = 0, \quad (1.10)$$

$$\nabla \cdot [\varepsilon(\mathbf{r}) \mathbf{E}(\mathbf{r}, t)] = 0, \quad (1.11)$$

$$\nabla \times \mathbf{H}(\mathbf{r}, t) - \varepsilon_0 \varepsilon(\mathbf{r}) \frac{\partial \mathbf{E}(\mathbf{r}, t)}{\partial t} = 0. \quad (1.12)$$

With (1.7) and (1.8), Maxwell's equations for $\mathbf{E}(\mathbf{r}, t)$ and $\mathbf{H}(\mathbf{r}, t)$ yield the equations

$$\frac{1}{\varepsilon(\mathbf{r})} \nabla \times [\nabla \times \mathbf{E}(\mathbf{r}, t)] + \frac{1}{c^2} \frac{\partial^2 \mathbf{E}(\mathbf{r}, t)}{\partial t^2} = 0, \quad (1.13)$$

$$\nabla \cdot \left[\frac{1}{\varepsilon(\mathbf{r})} \nabla \times \mathbf{H}(\mathbf{r}, t) \right] + \frac{1}{c^2} \frac{\partial^2 \mathbf{H}(\mathbf{r}, t)}{\partial t^2} = 0, \quad (1.14)$$

with $c = 1/\sqrt{\varepsilon_0 \mu_0}$.

The above-mentioned wave equations can be recast into a different form assuming the field pattern varies harmonically with time (*time-dependent solution*):

$$\mathbf{E}(\mathbf{r}, t) = \mathbf{E}(\mathbf{r}) \exp(-i\omega t), \quad (1.15)$$

$$\mathbf{H}(\mathbf{r}, t) = \mathbf{H}(\mathbf{r}) \exp(-i\omega t). \quad (1.16)$$

Then the *master equations* can be derived [13]:

$$\hat{\Theta}_E \mathbf{E}(\mathbf{r}) = \frac{\omega^2}{c^2} \mathbf{E}(\mathbf{r}) = \frac{1}{\varepsilon(\mathbf{r})} \nabla \times [\nabla \times \mathbf{E}(\mathbf{r})], \quad (1.17)$$

$$\hat{\Theta}_H \mathbf{H}(\mathbf{r}) = \frac{\omega^2}{c^2} \mathbf{H}(\mathbf{r}) = \nabla \times \left[\frac{1}{\varepsilon(\mathbf{r})} \nabla \times \mathbf{H}(\mathbf{r}) \right]. \quad (1.18)$$

The master equations constitute an eigenvalue problem. The \mathbf{H} -eigenvectors are allowed electromagnetic modes. $\mathbf{H}(\mathbf{r})$ is called eigenvector or eigenfunction of the $\hat{\Theta}_H$ operator. The eigenvectors $\mathbf{H}(\mathbf{r})$ and $\mathbf{E}(\mathbf{r})$ determine the spatial mode profile of the harmonic eigenmodes with frequency ω for a given structure $\varepsilon(\mathbf{r})$. The multiplicative constant $(\omega/c)^2$ is the *eigenvalue*.

Since $\hat{\Theta}_E$ and $\hat{\Theta}_H$ are linear operators the linear combination of two solutions is a solution of the eigenvalue problem. It should be noted that the eigenvalue problem has to fulfill the div-equations (1.1) and (1.3). Only $\hat{\Theta}_H$ is a Hermitian operator, see [13], but not $\hat{\Theta}_E$. Thus, $\hat{\Theta}_H$ has real eigenvalues, as opposed to $\hat{\Theta}_E$. Therefore, the master equation (1.18) is solved for \mathbf{H} . The electric field is calculated from (1.12) that can be written as

$$\nabla \times \mathbf{H}(\mathbf{r}, t) + i\omega\varepsilon_0\varepsilon(\mathbf{r})\mathbf{E}(\mathbf{r}, t) = 0. \quad (1.19)$$

The plain wave solution

One possible solution of the eigenvalue problem are plain waves $\mathbf{H}_{\mathbf{k}n}(\mathbf{r}) = \mathbf{H}_0 e^{i\mathbf{k}\cdot\mathbf{r}}$. For a given wave vector \mathbf{k} , an infinite number of discrete solutions can be found. They are labeled with increasing frequency using the *band number* n . Enforcing the transversality condition (1.1) leads to the connection between propagation vector \mathbf{k} and frequency ω by a dispersion relation

$$\omega(\mathbf{k}) = c\mathbf{k}/\sqrt{\varepsilon} = c\mathbf{k}/n(\mathbf{r}), \quad (1.20)$$

with the refractive index $n(\mathbf{r}) = \sqrt{\varepsilon(\mathbf{r})}$, real positive frequency ω , and *conserved* numbers $\mathbf{k} = (k_x, k_y, k_z)$ [14].¹ One corollary of the dispersion relation (1.20) is the group velocity

$$v_g = \frac{\partial\omega(\mathbf{k})}{\partial\mathbf{k}}. \quad (1.21)$$

Visualization of (1.20) can be done using the so-called *band diagram*, in which frequencies allowed by the dispersion relation (1.20) are plotted along a specified direction in \mathbf{k} -space [14]. We will rely on this concept at a later stage. The specified direction is denoted

¹The conservation of the wave vector rests upon the assumption of a uniform dielectric constant $\varepsilon(\mathbf{r})$ and invariance of Maxwell's equations under $r \rightarrow r' + r_0 \ \forall r_0$ [14].

by β , the propagation constant. Thus the dispersion relation reads now

$$\mathbf{k}_{\parallel} = \omega^2 \varepsilon - \beta^2, \quad (1.22)$$

with $\mathbf{k}_{\parallel} = (k_x, k_y, 0)$. Physically allowed states are denoted by (β, ω) .

Scaling properties

Another important feature of Maxwell's equations—the scaling properties shall be discussed briefly. To this end dimensionless variables are introduced:

$$\mathbf{r}' = \frac{1}{\gamma} \mathbf{r}, \quad (1.23)$$

$$\frac{c}{\gamma} t = t', \text{ with } \gamma \in \mathbb{R} \setminus \{0\}. \quad (1.24)$$

We define new functions

$$\varepsilon'(\mathbf{r}') = \varepsilon(\mathbf{r}), \quad (1.25)$$

$$\mathbf{E}'(\mathbf{r}', t') = \mathbf{E}(\mathbf{r}, t). \quad (1.26)$$

The scale-invariant master equation becomes

$$\frac{1}{\varepsilon'(\mathbf{r}')} \nabla' \times [\nabla' \times \mathbf{E}'(\mathbf{r}', t')] + \frac{1}{c^2} \frac{\partial^2 \mathbf{E}'(\mathbf{r}', t')}{\partial t'^2} = 0. \quad (1.27)$$

Once the harmonic modes of a system with given $\varepsilon(\mathbf{r})$ are known, the modes of a system differing by a constant factor γ everywhere may be obtained by simple rescaling.

1.1.2 Analogies from solid state physics

A characteristic property of photonic crystals is their periodic dielectric structure. In order to understand the photonic band structure, basic concepts of solid state theory will be reviewed briefly.

We start with a short survey of basic concepts, for a more comprehensive treatment, see [15]. The periodicity of solid matter is mathematically represented by a lattice vector

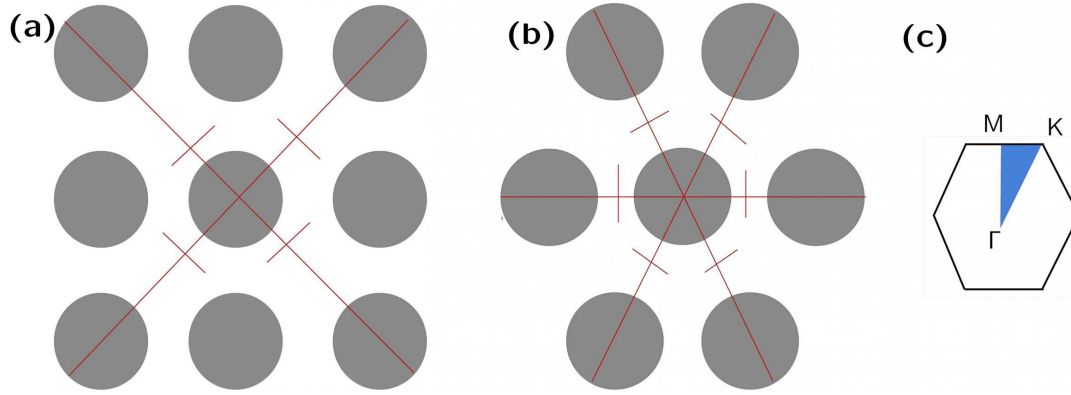


Figure 1.1: Construction of Wigner-Seitz cell for the (a) rectangular lattice, (b) hexagonal lattice. (c) Wigner-Seitz cell of (b) with irreducible Brillouin zone in blue. The *high symmetry points* of the BZ are Γ (center of BZ), K (middle of an edge joining two rectangular faces) and M (center of a rectangular face) [15].

of the form:

$$r_n = n_1 \mathbf{a} + n_2 \mathbf{b} + n_3 \mathbf{c}, \quad (1.28)$$

where $n_1, n_2, n_3 \in \mathbb{Z}$. \mathbf{a} , \mathbf{b} and \mathbf{c} are referred to as *lattice vectors*. Depending on the ratios of the lattice vectors and on their respective angles, lattices of different geometries can be obtained. It is, of course, possible to describe higher-dimensional objects by means of an appropriate set of basis vectors.

Reciprocal and direct lattice

How does the mathematical abstraction of a lattice relate to a crystal? Every point on the lattice (or *lattice point*) represents a group of atoms, the *basis*. A crystal is then completely characterized by lattice and basis. A unit cell of a given lattice is a cell consisting of a group of atoms possessing the symmetry of the crystal. When translated through all the vectors of the respective lattice, it covers the entire space. The minimal unit cell, i.e. the cell corresponding to a single lattice point, is the *primitive cell*. A special case of the primitive cell is the *Wigner-Seitz cell*, it is defined as the collection of points around a certain lattice point that are closer to that point than to any other point, see Figure 1.1. This type of cell represents the maximal symmetry of the crystal lattice. Of particular importance is the concept of the *reciprocal lattice* or *momentum*

space. A three-dimensional vector \mathbf{G} belongs to the reciprocal lattice if and only if

$$\mathbf{r}_n = n_1 \mathbf{a}_1 + n_2 \mathbf{a}_2 + n_3 \mathbf{a}_3, \quad (1.29)$$

where

$$\mathbf{G} \cdot \mathbf{r}_n = 2\pi n \text{ with } n \in \mathbb{Z}, \forall n_1, n_2, n_3 \text{ and } i \in \{1, 2, 3\} \quad (1.30)$$

and

$$\mathbf{G} = h\mathbf{g}_1 + k\mathbf{g}_2 + l\mathbf{g}_3. \quad (1.31)$$

Let's assume $n_1 = n_2 = 0$. Using (1.30) and (1.31) yields a straightforward relation between *direct* or original and reciprocal lattice

$$\mathbf{g}_i \cdot \mathbf{a}_j = 2\pi \delta_{ij} \quad (1.32)$$

since

$$(h\mathbf{g}_1 + k\mathbf{g}_2 + l\mathbf{g}_3) \cdot n_3 \mathbf{a}_3 = 0, \forall n_3. \quad (1.33)$$

The rules for constructing this lattice are contained in the orthogonality relation (1.32). It is a simple task to construct the basis vectors spanning the reciprocal lattice

$$\mathbf{g}_1 = 2\pi \frac{\mathbf{a}_2 \times \mathbf{a}_3}{\mathbf{a}_1 \cdot (\mathbf{a}_2 \times \mathbf{a}_3)}, \quad (1.34)$$

$$\mathbf{g}_2 = 2\pi \frac{\mathbf{a}_3 \times \mathbf{a}_1}{\mathbf{a}_2 \cdot (\mathbf{a}_3 \times \mathbf{a}_1)}, \quad (1.35)$$

$$\mathbf{g}_3 = 2\pi \frac{\mathbf{a}_1 \times \mathbf{a}_2}{\mathbf{a}_3 \cdot (\mathbf{a}_1 \times \mathbf{a}_2)}. \quad (1.36)$$

A special type of primitive cell is the *Brillouin zone* (BZ). It is defined as the Wigner-Seitz cell of the reciprocal lattice. Its importance lies in its ability to simplify the description of the solid. Calculations can be restricted to it. The concept of the *irreducible Brillouin zone* is related, see Figure 1.1; it is defined as the first Brillouin zone reduced by symmetries of the *point group* of the respective lattice. The three Brillouin zone points, Γ (middle of Brillouin zone), K (middle of an edge joining two rectangular faces) and M (center of a rectangular face) are *high symmetry points* of the hexagonal

lattice [15], see Figure 1.1. Later, band structures will be calculated along the k -space path $\Gamma - M - K - \Gamma$. Apart from them other high symmetry points exist.

Symmetries of photonic crystals

Photonic crystals can exhibit various symmetries. Some symmetries, however, are found in every photonic crystal; translational symmetry is the most prominent among them. Additionally to translational symmetry, other symmetry properties (like rotational and mirror symmetry) might exist [13]. The characteristic feature of crystals is their discrete translational symmetry.² We define a translation operator

$$\hat{T}_{\mathbf{R}} \psi(\mathbf{r}) = \psi(\mathbf{r} + \mathbf{R}). \quad (1.37)$$

The following explanations are based on [14]. With the definitions of the *in-plane* wave vector $\mathbf{k}_{\parallel} = (k_x, k_y, 0)$ and $\mathbf{r}_{\parallel} = (r_x, r_y, 0)$, assuming a system invariant under translations along vector \mathbf{R} with

$$\mathbf{R} = \mathbf{r}_{\parallel} + z\hat{\mathbf{z}} = h\mathbf{g}_1 + k\mathbf{g}_2 \text{ with } (\mathbf{g}_1, \mathbf{g}_2) \parallel \hat{\mathbf{z}} \text{ and } h, k \in \mathbb{N} \setminus \{0\}, \quad (1.38)$$

the eigenstates of a translation operator satisfy

$$\hat{T}_{\mathbf{R}} \psi(\mathbf{r}) = \psi(\mathbf{r} + \mathbf{R}) = C(h, k, z) \psi(\mathbf{r}). \quad (1.39)$$

Plane waves $\psi(\mathbf{r}) = \exp(i\beta z - i\mathbf{k}_{\parallel} \cdot \mathbf{r}_{\parallel})$ are eigenfunctions of (1.39). The respective eigenvalues are

$$C(h, k, z) = \exp(-i\beta z - i\mathbf{k}_{\parallel} \cdot \mathbf{r}_{\parallel}), \quad (1.40)$$

as can be seen easily. With the above-mentioned information it can be shown that $C(\mathbf{k}_{\parallel} + \mathbf{G}) = C(\mathbf{k}_{\parallel})$. Hence, the eigenstate of the translation operator (1.37) is degenerate for wave vectors of the form $\mathbf{k}_{\parallel} + \mathbf{G}$. The conserved parameters $(\mathbf{k}_{\parallel}, \beta)$ can be used as

²As an interesting note: The IUCR, the international union of crystallography has a more encompassing definition of crystals. Non-periodic structures are also included.

labels for the eigenstate of the translational operator:

$$\psi_{\beta, \mathbf{k}_{\parallel}}(\mathbf{r}) = e^{i\beta z + i\mathbf{k}_{\parallel} \cdot \mathbf{r}_{\parallel}} \sum_{\mathbf{G}} A_{\beta}(\mathbf{G}) e^{i\mathbf{G} \cdot \mathbf{r}_{\parallel}} = e^{i\beta z + i\mathbf{k}_{\parallel} \cdot \mathbf{r}_{\parallel}} U_{\beta}(\mathbf{r}_{\parallel}), \quad (1.41)$$

$$U_{\beta}(\mathbf{r}_{\parallel} + h\mathbf{g}_1 + k\mathbf{g}_2) = U_{\beta}(\mathbf{r}_{\parallel}), \quad (1.42)$$

with the expansion coefficients $A_{\beta}(\mathbf{G})$ defining a periodic function $U_{\beta}(\mathbf{r}_{\parallel})$ of transverse coordinates. Equations (1.41) and (1.42) are called BLOCH's theorem. Proofs of this important statement can be found in solid state physics textbooks, see [15] for instance.

Band structure

The existence of a photonic band structure is a direct consequence of the applicability of Bloch's theorem to photonic crystals. The reason for this band structure is the spatial variation of $\varepsilon(\mathbf{r})$ such that $\varepsilon(\mathbf{r}) = \varepsilon(\mathbf{r} + \mathbf{R})$. $\mathbf{R} = \sum_i p_i \mathbf{g}_i$ denotes a lattice vector, written as a sum of elementary lattice vectors $\{\mathbf{g}_i\}$ with $p_i \in \mathbb{N} \setminus \{0\}$. Bloch's theorem yields solutions that can be expressed as periodically modulated plane waves

$$\psi(\mathbf{r}) = u_{\mathbf{k}n}(\mathbf{r}) \exp(i\mathbf{k}\mathbf{r}), \text{ where } u_{\mathbf{k}n}(\mathbf{r}) = u_{\mathbf{k}n}(\mathbf{r} + \mathbf{R}). \quad (1.43)$$

Here, $\psi(\mathbf{r})$ is to be substituted with $\mathbf{E}(\mathbf{r})$, viz $\mathbf{H}(\mathbf{r})$. The eigenfrequencies $\omega_{\mathbf{k}n}$ of the various discrete solutions of (1.17) and (1.18) constitute the band structure. The vector \mathbf{k} is called the wave vector; it is related to the direction of motion of the photon in the crystal. The band index n numbers the energy bands in order of increasing frequency. The photonic band structure contains many information about the optical properties of photonic crystals. It can be obtained from the master equation using numerical methods. A convenient means to represent the band structure are band structure diagrams.

To obtain the actual band structure, numerical calculations are usually performed solving a master equation that accounts for the Bloch wave character of the wave functions in \mathbf{k} -space. This master equation can be derived by inserting the Bloch theo-

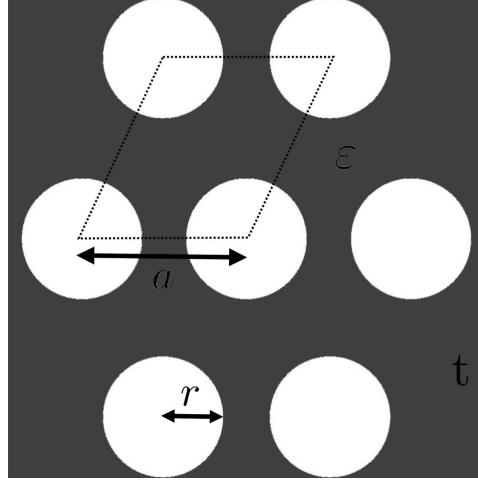


Figure 1.2: Visualization of photonic crystal slab with air holes with radius r . The air holes are distributed on a hexagonal lattice with lattice constant a and thickness t . All photonic crystals in this thesis have a hexagonal lattice.

rem (1.41) and (1.42) in the master equation (1.18):

$$\begin{aligned}\hat{\Theta}_H \mathbf{H}_k &= \left(\frac{\omega(\mathbf{k})}{c} \right)^2 \mathbf{H}_k \\ \nabla \times \varepsilon(\mathbf{r})^{-1} \times e^{i\mathbf{k} \cdot \mathbf{r}} \mathbf{u}_{kn}(\mathbf{r}) &= \left(\frac{\omega(\mathbf{k})}{c} \right)^2 e^{i\mathbf{k} \cdot \mathbf{r}} \mathbf{u}_{kn}(\mathbf{r}) \\ (i\mathbf{k} + \nabla) \times \varepsilon(\mathbf{r})^{-1} (i\mathbf{k} + \nabla) \times \mathbf{u}_{kn}(\mathbf{r}) &= \left(\frac{\omega(\mathbf{k})}{c} \right)^2 \mathbf{u}_{kn}(\mathbf{r}) \\ \hat{\Theta}_H^k \mathbf{H}_k \mathbf{u}_{kn} &= \left(\frac{\omega(\mathbf{k})}{c} \right)^2 \mathbf{u}_{kn}(\mathbf{r})\end{aligned}$$

with the new operator

$$\hat{\Theta}_H^k = (i\mathbf{k} + \nabla) \times \varepsilon(\mathbf{r})^{-1} (i\mathbf{k} + \nabla) \times . \quad (1.44)$$

Once we calculate $\omega(\mathbf{k})$, the dispersion characteristics of the photonic crystal are known. The calculation of $\omega(\mathbf{k})$ is greatly simplified by symmetry considerations since \mathbf{k} will be calculated in the *irreducible Brillouin zone* only.

1.1.3 Planar photonic crystals

The properties and relations discussed till now hold basically for all dielectric periodic meta materials. In this section we shall deal with specific properties of planar photonic crystals.

Two-dimensional photonic crystals

Three-dimensional photonic crystals may display a complete three-dimensional photonic crystal band gap. Fabrication of these structures, however, is complicated. Therefore, the main focus of today's photonic crystals research is on two-dimensional photonic crystal slabs; i.e. two-dimensional photonic crystals with a finite thickness. While different designs have been proposed and realized [13], the most well-known design is the hexagonal photonic crystal slab with air holes, see Figure 1.2. The substrate has a thickness t , dielectric constant ε , lattice constant a and the air holes have radius r . The band diagrams were calculated using the open-source software package MPB (*MIT Photonic Band package*), [11]. It is probably one of the most popular programs solving Maxwell's equations in the frequency space, see Sec. 1.2.5 for details.

Considering two-dimensional systems has the advantage of further simplifications through symmetries. The mirror symmetry with respect to the z axis allows only two types of modes if $\mathbf{k} \perp \hat{\mathbf{z}}$ [13], viz: even and odd modes. The symmetry relations imply that the only non-vanishing contributions for even modes are E_x , E_y and H_z , while odd modes have the components H_x , H_y and E_z . The nomenclature *transverse electric* modes (TE) for the former mode polarization and *transverse magnetic* for the later (TM) polarization is used. Strikingly, TE and TM polarized electric modes do not interact [13].

Light guiding in photonic crystals

In electronics, so-called electron guiding is done by thin metal wires. Obviously, a different method has to be used for light guiding. Traditionally, index guiding based on *total internal reflection* (TIR) is used. Photonic crystals, however, offer an additional mechanism to 'mold the flow of light'[13].

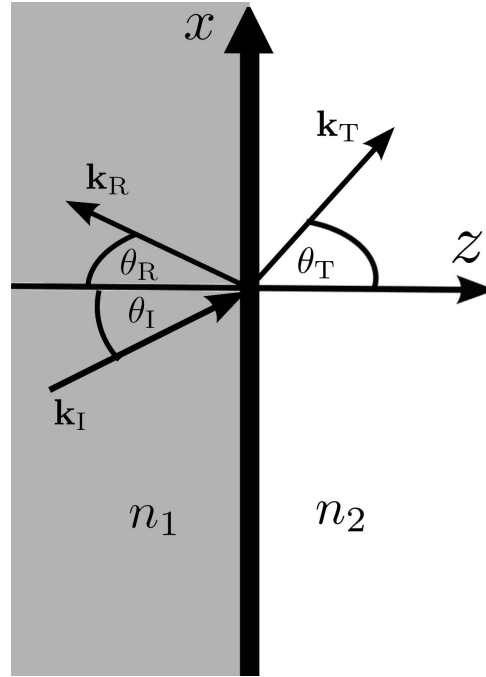


Figure 1.3: Diffraction at a flat interface between two dielectrics with refractive indices n_1 , and n_2 . The parallel component \mathbf{k}_{\parallel} of \mathbf{k} is a conserved quantity as implied by Snell's law. The angles θ_I , θ_R and θ_T represent angles of incidence, refraction and transmission, respectively.

Let us first review the classic mechanism of index guiding as it is used in optical fibers for instance [13]. According to SNELL's law:

$$n_1 \sin \theta_I = n_2 \sin \theta_T. \quad (1.45)$$

If $n_1 > n_2$ and $\theta_I > \theta_T$, where θ_c denotes the critical angle, total internal reflection occurs. So, total internal reflection occurs only within in the higher-index medium. Light can be guided through this mechanism. The critical angle is given by

$$\theta_c = \arcsin n_1/n_2. \quad (1.46)$$

On a more abstract level, Snell's law can be considered a special case of two conservation laws [13]; the conservation of frequency ω (a corollary to linearity and time-invariance of Maxwell's equations), and conservation of the parallel component \mathbf{k}_{\parallel} of \mathbf{k} . More practically, $\mathbf{k}_{\parallel} = \mathbf{k} \sin \theta$ and $k = n\omega/c$ form the dispersion relation. Setting the parallel component of \mathbf{k} equal on both sides results in Snell's law (1.45). This approach has the advantage of generality as we will see soon.

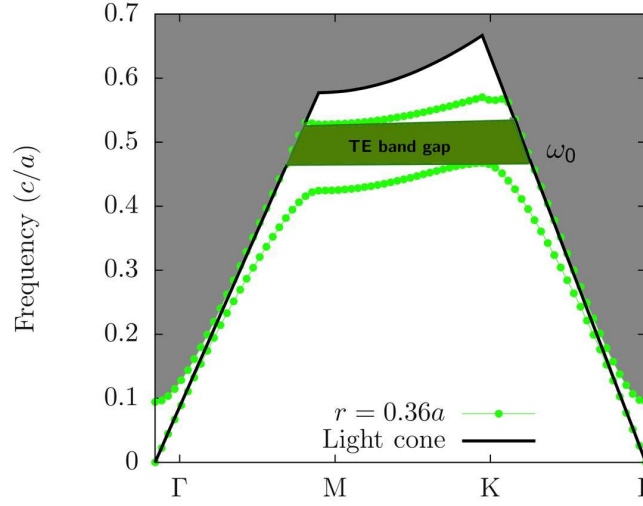


Figure 1.4: Projected band structure diagram of silicon nitride with air holes on a hexagonal lattice. Only the dielectric and the air band are shown. Only TE modes are shown. Note the band gap for guided modes. The shaded region indicates the frequencies of states when vertical propagation is permitted.

Figure 1.4 consists of two parts, the shaded area, and below, the non-obscured area. Modes that are not confined to the medium extending out to infinity (*lossy modes*), are obscured in the shaded area. In the limit far away from the medium, plane waves are a good approximation for these modes. The frequency of these modes is given by $\omega = ck = c\sqrt{k_{\parallel}^2 + k_{\perp}^2}$ for a fixed value of k_{\parallel} ; k_{\perp} , however, is not conserved and can take any value. Setting $k_{\perp} = 0$ we get the *light line*. It separates the light cone, that is the region of the band structure with $\omega > ck_{\parallel}$, i.e. extended states and the continuous modes. The former are solutions of Snell's law. Solutions below the light cone do exist, they are discrete solutions with the following perpendicular wave vector component: $k_{\perp} = \pm i\sqrt{k_{\parallel}^2 - \frac{\omega^2}{c^2}}$, which implies that they are decaying exponentially into the air for $z \rightarrow \infty$. They are called *index-guided* modes.

Photonic band gap

One particular similarity between solid state crystals and photonic crystals has been explained in the previous section, now we will focus on a further feature shared by both, the band gap. In solid state physics, the band gap or stop band is an energy region with zero probability of finding a particle there. A *photonic band gap* (PBG) is a frequency band forbidding all electromagnetic waves inside it, at least in principle. No purely

real \mathbf{k} may exist in the band gap; evanescent, exponentially decaying modes, however, are allowed.

So as to give an example of the astonishing consequences of the photonic band gap, we will consider spontaneous emission. The effect of *inhibited spontaneous emission* is first described by [18].³ Recall that spontaneous emission is a transition of an electron from an initial state represented by $|u_i\rangle$ to a final state represented by $|u_f\rangle$. According to FERMI's *golden rule*, the transition probability from state i to state f with density of states $\rho(E)$ per unit energy is given by

$$\frac{2\pi}{\hbar} \rho(E_f) |\langle u_i | H' | u_f \rangle|^2, \quad (1.47)$$

with H' being the Hamiltonian describing an interaction treated as a perturbation and $\langle u_i | H' | u_k \rangle$ being the matrix element between initial and the final state. What happens if $\rho(E_f) = 0$, i.e. the density of optical modes for the final states vanishes? Obviously, no spontaneous emission will take place. The idea put forward in [18] gave rise to research focusing on creating photonic band gap materials. Spontaneous emission is inhibited in the photonic band gap region. To show analytically (or semi-analytically) the existence of a one-dimensional band gap is possible, for two and three dimensions; the calculations are cumbersome [14]. In two-dimensional photonic crystals there may be band gaps for the TE or TM polarizations, but not for both. If the periodic pattern is realized using air holes, only a TE photonic band gap will be found, see Figure 1.4 [13]. Three-dimensional materials may exhibit a complete band gap, but this comes at the cost of more complex fabrication [9, 13].

Photonic crystal structures

The photonic crystals considered so far exhibit a photonic band gap for modes confined to the photonic crystal (guided modes) caused by the strictly periodic arrangement of holes.

It has been mentioned that two-dimensional photonic crystals may exhibit a band-gap for guided modes, see Figure 1.4. The perfect translational symmetry of the photonic crystal is the reason for the photonic band gap. It can be broken by locally adding or removing dielectric material. Interestingly, the former change gives rise to donor modes

³E. M. Purcell mentions in a paper [19] already in 1946 the possibility of controlling spontaneous emission.

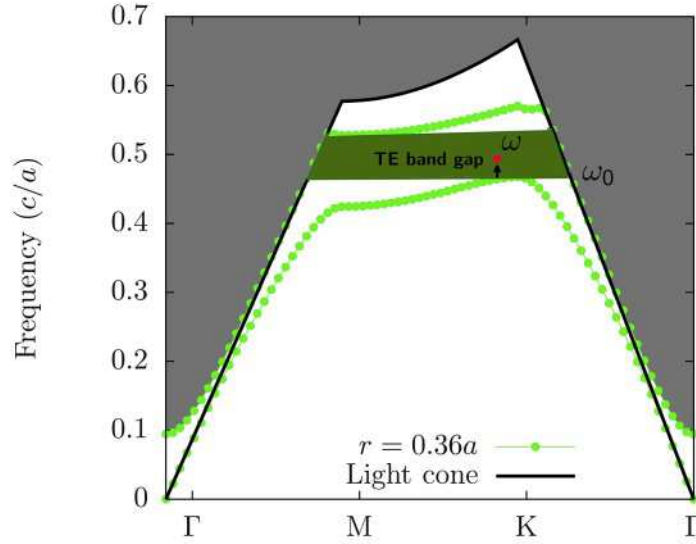


Figure 1.5: Projected band structure of Si_3N_4 with air holes on hexagonal lattice and with point defect. Note the band gap with allowed states at $\omega = \omega_0$. Only TE modes are shown. The shaded region indicates the frequencies of states when vertical propagation is permitted.

at the bottom of the conduction band; the latter change introduces acceptor modes at the top of the dielectric band [20]. Defects break the translational symmetry and introduce localized states with frequency ω_0 (and frequency width $\Delta\omega$) into the band gap.

One prominent cavity design is the *L3* cavity. It is constructed by removing three consecutive holes in a row [21], see Figure 1.6 (b). The *W1* photonic crystal waveguide is created by removing an entire line of holes from the hexagonal lattice, i.e. by forming a linear defect, see Figure 1.6 (a). Different ways exist to implement a linear defect, with the only condition being translational symmetry in one direction [13]. The light guiding is based on the photonic band gap of the surrounding crystal [13]. Apart from these two structures many others exist.

1.1.4 Resonant cavity parameters

A photonic cavity can be seen as a device trapping light of given frequency (width) for a certain time. The correspondence between trapping time and spectral width is established through a Fourier transform. The most important optical property of the photonic crystal cavity is the *quality factor* Q for a given resonance frequency ω_c . Dif-

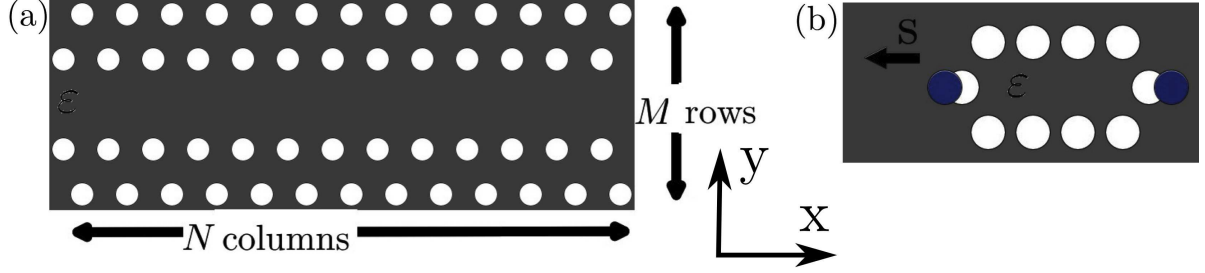


Figure 1.6: Two different PC structures. (a) *W1* waveguide. (b) *L3* cavity with outer cavity holes displace by distance s .

ferent equivalent definitions exists [13]:

$$Q = \frac{\omega_c U}{P} = \frac{\omega_c}{\kappa} = \frac{\omega_c}{\Delta\omega}. \quad (1.48)$$

Here, U is the electromagnetic energy stored in the mode with frequency ω_c ; $\Delta\omega$ denotes the *full width half measure* (FWHM). The electromagnetic energy is defined as:

$$U = \frac{1}{2} \int_V d\mathbf{r} [\varepsilon_0 \varepsilon(\mathbf{r}) |\mathbf{E}(\mathbf{r})|^2 + \mu_0 \mu(\mathbf{r}) |\mathbf{H}(\mathbf{r})|^2]. \quad (1.49)$$

We can interpret $1/Q$ in different ways. P describes the energy leaking out of the corresponding cavity, i.e. the power loss. Therefore, $1/Q$ may be seen as the decay rate. On the other hand, $1/Q$ is also a lifetime. After a cycle $T = 2\pi/\omega_c$, the field intensity

$$I(t) = I_0 \exp(-\kappa t) \quad (1.50)$$

decayed to

$$I(T) = I_0 \exp(-2\pi), \quad (1.51)$$

with the loss rate κ . The shape of the cavity resonance, i.e. intensity over frequency, yields a Lorentzian intensity distribution which is the Fourier transform of a decaying exponential function. The quality factor can be obtained as the ratio of ω_c to $\Delta\omega$.

Two types of contributions can be distinguished for planar photonic crystals:⁴ *In-plane losses* P_{\parallel} due to coupling to guided modes in the slab, and *out-of-plane losses* P_{\perp}

⁴Other losses are neglected here.

due to coupling to radiative modes. Since $P = P_{\perp} + P_{\parallel}$, it follows with (1.48)

$$\frac{1}{Q} = \frac{1}{Q_{\parallel}} + \frac{1}{Q_{\perp}}. \quad (1.52)$$

Apart from the quality factor, the *modal volume* V_{eff} , a measure for the localization of a mode in space, is of paramount importance. It is defined as [13]

$$V_{\text{eff}} = \frac{\int d^3\mathbf{r} \varepsilon |\mathbf{E}|^2}{\max \varepsilon |\mathbf{E}|^2}, \quad (1.53)$$

even though differing definition are used sometimes. Typically, V_{eff} is given in units of $(\lambda/n)^3$ with $n = \sqrt{\max \varepsilon}$. Q and V_{eff} represent spatial and spectral confinement. Both should be taken into account simultaneously when optimizing a cavity design. Depending on the usage of the particular photonic crystals Q/V_{eff} (weak coupling regime) [22], $Q/\sqrt{V_{\text{eff}}}$ (strong coupling regime) [23] or Q^2/V_{eff} (nonlinear optics) [24] have to be maximized [25]. There is an inverse relation between real space volume and Fourier space volume. A large Fourier space volume entails more losses through total internal reflection (out-of-plane losses).

Optimization of Q

Increasing Q comes often at cost of increasing V_{eff} . The modal volume of photonic crystal cavities, however, is inherently small [26], i.e. $V_{\text{eff}} \approx (\lambda/n)^3$ as opposed to the quality factor that may be increased by reducing out-of-plane losses [26]. Increasing the later is indeed one of the aims of our work while there is only limited space to reduce V_{eff} .

Unfortunately, we will not be able to offer a general recipe how to find the optimal trade-off between high Q and low modal volume.⁵ It has been shown [27] that knowledge of the \mathbf{k} wave vector distribution for a given cavity mode is instrumental in improving the quality factor of photonic crystal cavities [21]. Indeed, the method to increase Q applied by [21] is *gentle confinement*. The intensity pattern $|\mathbf{E}|^2$ should resemble a Gaussian envelope to minimize radiation losses. Displacement of the inner cavity holes and lowering their radius improve the intensity pattern resemblance significantly [25].

⁵See [22] for a general recipe for designing high- Q and low- V two-dimensional photonic crystal cavities.

1.2 The nitrogen vacancy center of diamond

Now, we will introduce the probably most prominent solid state single photon source operated at room temperature, the nitrogen vacancy (NV) center of diamond. Possible applications in conjunction with PCs exist in the field of quantum computing, quantum cryptography, quantum electrodynamics (QED) and many other areas of modern research.

The NV center of diamond, a point defect, is one of more than 100 luminescent defect states in diamond. The defect consists of a nearest-neighbor pair of a lattice vacancy (V) and of a nitrogen (N) atom, substituting for a carbon atom, see Figure 1.7. The nitrogen rich type Ib diamond may exhibit the NV defect center after irradiation damage. The strong absorption at 1.945 eV (637 nm) is caused by the defect. At low temperatures the absorption line takes the form of a narrow optical resonance, the zero phonon line (ZPL), see [28] for a review of defect centers in diamond. Unfortunately, the NV center of diamond suffers from the major draw-back of weak coupling to the electric field compared to quantum dots for instance [29]. Coupling the NV defect center into a nanocavity (e.g. a photonic crystal) may be used to increase the spontaneous emission rate (*PURCELL effect*). The rate of spontaneous emission is increased by the *Purcell factor* F [19]:

$$F = \frac{3}{4\pi^2} \left(\frac{\lambda_c}{n} \right)^3 \frac{Q}{V_{\text{eff}}}, \quad (1.54)$$

with the cavity resonance wavelength λ_c , the quality factor Q and the modal volume V_{eff} . The above-mentioned equation adds an additional motivation to increase Q/V_{eff} .

1.3 Numerical methods

After the brief introduction of the theoretical background required, we focus on the numerical methods that were used to obtain the results. The *finite-difference time-domain* (FDTD) method is described in [30] and in the appendix to [13]. Only a short introduction can be offered in the limited scope of this thesis. Three methods, *the plane waves method*, the finite-difference time-domain method, and the *finite-difference frequency-domain method* will be introduced.

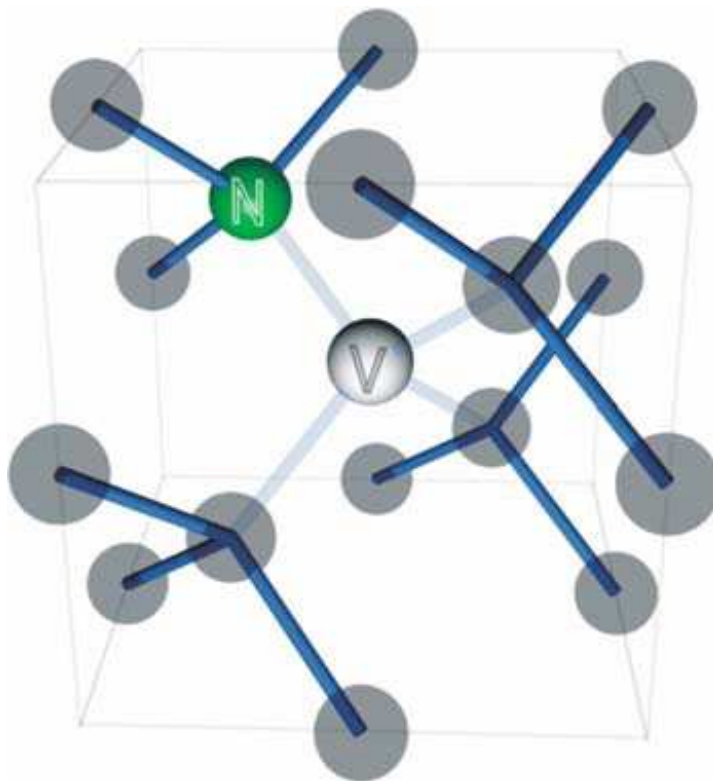


Figure 1.7: Schematic representation of NV center structure. Notice the nitrogen (N) atom and the vacancy (V) in lieu of the carbon atoms. From [28].

1.3.1 General overview of different methods

Roughly speaking, three categories of problems exist in computational photonics [13]:

1. **Time-domain simulations:** start with a time-dependent current distribution $\mathbf{J}(\mathbf{x}, t)$ and simulate the fields $\mathbf{E}(\mathbf{x}, t)$ and $\mathbf{H}(\mathbf{x}, t)$ as they propagate in time.
2. **Frequency-domain responses:** find the fields caused by a given current distribution $\mathbf{J}(\mathbf{x}) \exp(-i\omega_0 t)$ at a fixed frequency ω_0 . So as to find the field, the problem is rephrased using linear algebra: $Ax = b$, this equation is to be solved for x .
3. **Frequency-domain eigenproblems:** solve the eigenproblem $Ax = \omega^2 Bx$ with the band structure $\omega(\mathbf{k})$ being the eigenvalue, and the eigenvector x . Techniques from the field of linear algebra are applied.

When calculating band structures, the last method will be used (as we did). On the other hand, some problems may require knowledge of a transmission and reflection spectrum, information that is not easily obtained from the band structure. Alternatively, classification of the methods follows the type of method used to reduce the infinite number of unknowns of the *partial differential equations* (PDE) to a finite value [13].

1.3.2 The plane wave expansion method

The following explanations are based on [14], see there for a more detailed description. Bloch's theorem implies that the modal fields $\mathbf{E}_{\mathbf{k}}$ and $\mathbf{H}_{\mathbf{k}}$ can be written as the product of a complex exponential and a periodic modulation function. Thus, they take the following form:

$$\mathbf{H}_{\mathbf{k}}(\mathbf{r}) = \sum_{\mathbf{G}} \mathbf{H}_{\mathbf{k}}(\mathbf{G}) \exp(i(\mathbf{k} + \mathbf{G}) \cdot \mathbf{r}). \quad (1.55)$$

Similarly, the periodic dielectric constant ε can be expanded:

$$\frac{1}{\varepsilon(\mathbf{r})} = \sum_{\mathbf{G}} \kappa(\mathbf{G}) \exp(i\mathbf{G} \cdot \mathbf{r}). \quad (1.56)$$

Maxwell's equations in terms of \mathbf{E} and \mathbf{H} [14]:

$$\omega^2 \mathbf{E} = \frac{1}{\varepsilon(\mathbf{r})} \Delta \times (\Delta \times \mathbf{E}), \quad (1.57)$$

$$\Delta \cdot \varepsilon(\mathbf{r}) \mathbf{E} = 0, \quad (1.58)$$

$$\omega^2 \mathbf{H} = \Delta \times \left(\frac{1}{\varepsilon(\mathbf{r})} \Delta \times \mathbf{H} \right), \quad (1.59)$$

$$\Delta \cdot \mathbf{H} = 0. \quad (1.60)$$

The fields $\mathbf{v}_{\mathbf{k}n}(\mathbf{r})$ and the reciprocal dielectric constant $1/\varepsilon(\mathbf{r})$ are expanded into a discrete set of plane waves:

$$\varepsilon^{-1}(\mathbf{r}) = \sum_{\mathbf{G}} \kappa(\mathbf{G}) e^{i\mathbf{G} \cdot \mathbf{r}}, \quad (1.61)$$

$$\mathbf{v}_{\mathbf{k}n}(\mathbf{r}) = \tilde{\mathbf{v}}_{\mathbf{k}n}(\mathbf{G}) e^{i\mathbf{G} \cdot \mathbf{r}}. \quad (1.62)$$

For a given \mathbf{k} these equations present a linear eigenvalue problem with eigenvalue (modal frequency) ω_k with the Fourier coefficients $\tilde{\mathbf{v}}_{\mathbf{k}n}(\mathbf{G})$ and $\kappa(\mathbf{G})$. To evaluate the equation, only a finite number N of Fourier coefficients will be calculated. Unphysical solutions have to be excluded by enforcing the transversality conditions (1.60) and (1.58). Inserting (1.61) and (1.62) in (1.55) yields the following set of linear eigenvalue equations [25]:

$$\sum_{\mathbf{G}'} \kappa(\mathbf{G} - \mathbf{G}') (\mathbf{k} + \mathbf{G}) \times [(\mathbf{k} + \mathbf{G}') \times \tilde{\mathbf{v}}_{\mathbf{k}n}(\mathbf{G}')] = -\frac{\omega_{\mathbf{k}n}^2}{c^2} \tilde{\mathbf{v}}_{\mathbf{k}n}(\mathbf{G}). \quad (1.63)$$

A suitable set of vectors \mathbf{G} has to be chosen; with the help of iterative solvers it is possible to calculate the coefficients $\tilde{\mathbf{v}}_{\mathbf{k}n}(\mathbf{G})$ [25]. The plane wave expansion method operates in the frequency domain; eigenfrequencies $\omega_{\mathbf{k}n}$ and eigenvectors $\mathbf{H}_{\mathbf{k}n}$ are therefore readily calculated. MPB is based on the plane wave expansion method, it was used to calculate the band structures in this thesis. It is a *finite-difference* method, as shall be explained now.

1.3.3 Finite differences

Different numerical methods exist to discretize (partial) differential equations, i.e. to reduce the number of unknowns. We start with the Taylor expansion of a sufficiently

smooth function $u(x)$:

$$u(x+h) = u(x) + u'(x)h + \mathcal{O}(h^2), \quad (1.64)$$

$$u(x-h) = u(x) - u'(x)h + \mathcal{O}(h^2). \quad (1.65)$$

Subtracting the two formulae yields the *centered difference formula*:

$$u'(x) = \frac{u(x+h) - u(x-h)}{2h} + \mathcal{O}(h^2). \quad (1.66)$$

This is a second order approximation, it is used by the following method.

1.3.4 The finite-difference time-domain method

We give a short overview over the finite-difference time-domain (FDTD) method and its applications to photonic crystal structures. As implied by the name of the numerical method, it operates in the time-domain using a time-dependent current-distribution as an input parameter. The temporal propagation of the electromagnetic fields is given by two curl equations, i.e. differential equations. The basic idea of the the YEE Algorithm (YA) is to transform the two Maxwell's equations

$$\Delta \times \mathbf{H} = c^{-1} \left(\mathbf{J} + \varepsilon_r \frac{\partial \mathbf{E}}{\partial t} \right), \Delta \times \mathbf{E} = -c^{-1} \frac{\partial \mathbf{H}}{\partial t}, \quad (1.67)$$

in a rectangular coordinate system into equations that are solvable by additions and multiplications only [31]. It follows from Maxwell's equations (source-free):

$$\frac{\partial E_z}{\partial t} = \frac{1}{\varepsilon} \left(\frac{\partial H_y}{\partial x} - \frac{\partial H_x}{\partial y} \right), \frac{\partial H_z}{\partial t} = -\frac{1}{\mu} \left(\frac{\partial E_y}{\partial x} + \frac{\partial E_x}{\partial y} \right), \quad (1.68)$$

$$\frac{\partial E_y}{\partial t} = \frac{1}{\varepsilon} \left(\frac{\partial H_x}{\partial z} - \frac{\partial H_z}{\partial x} \right), \frac{\partial H_y}{\partial t} = -\frac{1}{\mu} \left(\frac{\partial E_x}{\partial z} + \frac{\partial E_z}{\partial x} \right), \quad (1.69)$$

$$\frac{\partial E_x}{\partial t} = \frac{1}{\varepsilon} \left(\frac{\partial H_z}{\partial y} - \frac{\partial H_y}{\partial z} \right), \frac{\partial H_x}{\partial t} = -\frac{1}{\mu} \left(\frac{\partial E_z}{\partial y} + \frac{\partial E_y}{\partial z} \right). \quad (1.70)$$

To evaluate the above-mentioned equations, they are rewritten in differential form:

$$\frac{\partial f}{\partial x} \rightarrow \lim_{h \rightarrow 0} \frac{f(x+h) - f(x-h)}{2h} \stackrel{\text{def}}{=} d_x f. \quad (1.71)$$

More accurate results will be obtained, evaluating the electromagnetic fields at half

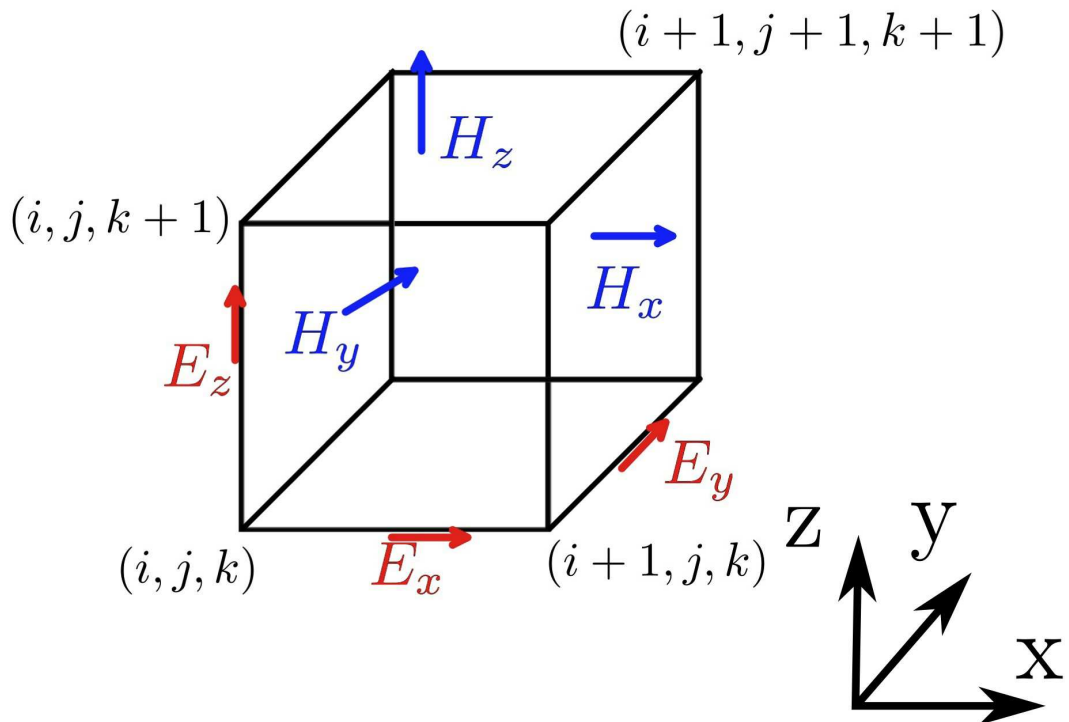


Figure 1.8: Schematic visualization of electric and magnetic fields as they are calculated in the Yee Algorithm. Note that \mathbf{E} and \mathbf{H} are staggered so that there is half a time-step between the update of \mathbf{E} and \mathbf{H} .

time steps, i.e. the leapfrog algorithm is used:

$$\frac{f(x + h/2) - f(x - h/2)}{h} \stackrel{\text{def}}{=} d_x f. \quad (1.72)$$

The Yee Algorithm is a leapfrog algorithm calculating $\mathbf{E}(t)$ from $\mathbf{E}(t - \Delta t)$ and $\mathbf{H}(t + \Delta t/2)$ from $\mathbf{H}(t - \Delta t/2)$. Regarding the notation we follow [31]; a grid point in space and time is denoted as

$$(i, j, k; t) = (i\Delta x, j\Delta y, k\Delta z; n\Delta t). \quad (1.73)$$

The respective function will be cast into the following form

$$F(i\Delta x, j\Delta y, k\Delta z, n\Delta t) = F^n(i, j, k). \quad (1.74)$$

The derivative $\partial H_x / \partial t$ can be written as

$$\begin{aligned} & \frac{H_x^{n+1/2}(i, j + \frac{1}{2}, k + \frac{1}{2}) - H_x^{n-1/2}(i, j + \frac{1}{2}, k + \frac{1}{2})}{\Delta t} \\ &= \frac{E_y^n(i, j + \frac{1}{2}, k + \frac{1}{2}) - E_z^n(i, j + \frac{1}{2}, k)}{\Delta z} \\ & \quad - \frac{E_z^n(i, j + 1, k + \frac{1}{2}) - E_z^n(i, j, k + \frac{1}{2})}{\Delta y}. \end{aligned} \quad (1.75)$$

Analogously, an equation can be constructed for the electric field derivatives [31].

In the FDTD method, a finite grid is used, this *volume discretization* leads to an important question: how to perform the termination of the computational region without introducing significant artifacts. For periodic structures, periodic boundary conditions are the natural choice. Once the periodicity is broken, by a defect for instance, periodic boundary conditions or a hard wall will lead to unacceptable artifacts caused by reflections from the boundary if the problem involves wave equations [13]. A remedy was suggested by BERENGER [32]. He proposed an absorbing boundary layer, the *perfectly matched layer* (PML) consisting of conductive material that attenuates an incoming wave exponentially. The software used for numerical band structure calculations is MEEP. It uses *uniform perfectly matched layers* (UPML). Besides the grid boundary, the grid size is important as the electromagnetic fields should not change much over one

time step. This condition is the COURANT criterion [33]:

$$\sqrt{(\Delta x)^2 + (\Delta y)^2 + (\Delta z)^2} > c_{\max} t. \quad (1.76)$$

An additional difficulty arises from the fact that most FDTD implementations use the orthogonal Yee cell. Thus the practical question of modeling a curved surface on a rectangular lattice has to be asked. A technique called *sub-pixel averaging* [34, 35] is used for this.

At this point, we want to return to the main task of the simulations, the extraction of resonant modes and the optimization of the cavities for a given radiation mode. A tool called `Harminv` is applied. It is a free program solving the problem of *harmonic inversion*. A finite-length and discrete-time signal $f(t)$ is given in a specified bandwidth. `Harminv` determines the frequencies ω_k , decay constants α_k , phases ϕ_k and amplitudes A_k of the sinusoids [36, 37]

$$f(t) = \sum_k A_k \sin(\omega_k t + \phi_k) e^{-\alpha_k t}. \quad (1.77)$$

The method operates with higher accuracy than *fast Fourier transform* (FFT) as `Harminv` rests upon the assumption that the signal consists of only a small number of decaying and oscillating modes with a certain amount of noise.

The electromagnetic source used in MEEP have different parameters. All sources used in MEEP are *current sources*, i.e. they specify \mathbf{J} but not a particular electric or magnetic field. A point-dipole source is default, its size can be changed. The time-dependence of the source can be set to be either continuous ($\propto \exp(i\omega t)$), Gaussian ($\propto \exp(-i\omega t - (t - t_0)^2/2w^2)$) or custom (any $f(t)$). The standard position of the source is the center of the simulated area. Symmetries can be exploited; this will reduce the amount of computation and storage required for simulation.

1.3.5 The finite-difference frequency-domain method

The basic idea of the algorithm is to transform the Maxwell Hamiltonian eigenvalue problem to a standard linear algebra problem. Using (1.44) the source-free Maxwell's equation for a linear dielectric (1.14) reads:

$$\hat{A}_{\mathbf{k}} |\mathbf{H}_{\mathbf{k}}\rangle = (\omega/c)^2 |\mathbf{H}_{\mathbf{k}}\rangle \quad \text{with} \quad |\mathbf{H}_{\mathbf{k}}\rangle = e^{i\mathbf{k}\cdot\mathbf{r}-\omega t} |H_{\mathbf{k}}\rangle. \quad (1.78)$$

For a fixed \mathbf{k} , orthogonality of the modes can be enforced:

$$\left\langle \mathbf{H}_{\mathbf{k}}^{(n)} \left| \mathbf{H}_{\mathbf{k}}^{(m)} \right. \right\rangle = \delta_{n,m}. \quad (1.79)$$

In order to solve (1.78), a final expansion of the states in a basis $\{|a_m\rangle\}$ is conducted:

$$|\mathbf{H}_{\mathbf{k}}\rangle \approx \sum_{m=1}^N a_m |a_m\rangle. \quad (1.80)$$

Expression (1.80) becomes exact for $N \rightarrow \infty$ thereby completing the basis. Then, (1.80) becomes a standard linear algebra eigenproblem

$$Ah = \left(\frac{\omega}{c}\right)^2 Bh, \quad (1.81)$$

where h is a column vector with basis coefficients h_m . A and B are $N \times N$ matrices with respective entries $A_{lm} = \langle a_l | \hat{A}_{\mathbf{k}} | a_m \rangle$ and $B_{lm} = \langle a_l | a_m \rangle$. To exclude unphysical solutions, the transversality constraint (1.3) has to be enforced. The exact algorithm with its optimizations is described in detail in [11].

This chapter offered a short introduction into the physics behind photonic crystals, i.e. a short review of Maxwell's equations applied to periodic dielectric media and basic notions of solid state physics. The physics of the NV center were briefly introduced. In the second part we outlined the basic numeric methods used. The next step is performing the actual simulations.

Chapter 2

Photonic Crystal Simulations

After having reviewed the basic properties of photonic crystals (PC) and the methods to simulate and fabricate them in the last chapter, this chapter focuses on the results of the simulations.

First we simulate band structures and optimize the band gap size (Sec. 2.1) of defect-less PC slabs, then we concentrate on optimizing the Q -factor (Sec. 2.2.1) of $L3$ cavities. Finally, the Q -factor of a nanocavity realized by local width modulation of a line defect is optimized (Sec. 2.2.2).

All structures are based on silicon nitride (Si_3N_4) with approximately $n = 2.01$ for $\lambda = 637 \text{ nm}$, see Sec. 1.2, with a hexagonal lattice of air holes. Two-dimensional PC slabs operating in the visible spectral range are considered attractive tools with applications in several fields [38]. The band gap and later the quality factor Q are optimized. We consider *suspended membrane* structures surrounded entirely by air. The influence of a substrate is discussed in [13, 39] among others.

A few words on units

Both simulation tools, MPB as well as MEEP, use the scale-invariance of Maxwell's equations. Thus, if all system sizes are multiplied by a constant a , the respective solutions of Maxwell's equations have to be multiplied accordingly. Naturally, the basic constant is the lattice constant a . Therefore all units that are relevant for us are expressed in terms of the lattice constant, i.e. a normalized to unity. Following the practice of theoretical physicists, constants like c , μ_0 and ε_0 are normalized to unity. As $c = 1$, it follows that

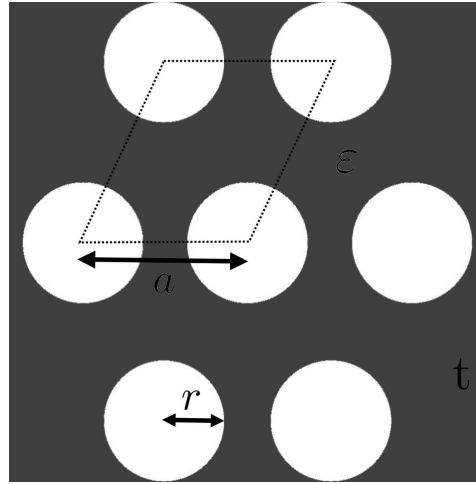


Figure 2.1: Visualization of PC slab with air holes. The air holes are distributed on a hexagonal lattice. All PCs in this thesis have a hexagonal lattice. Radius r , lattice constant a and thickness t can be varied. Note that no PML is necessary as periodic boundary conditions can be used.

the frequency f is always specified in units of c/a , or equivalently ω in units of $2\pi c/a$; see Sec. 1.1.1.

2.1 Finite-difference frequency-domain simulations

MPB simulations were performed primarily to obtain an overview about the band structure and band gap sizes of perfect, i.e. defect-less hexagonal Si_3N_4 PC slabs with air hole radius r , slab-thickness t , dielectric constant ε , and lattice constant a as depicted in Figure 2.1.

2.1.1 The influence of the resolution

The simulation tool MPB belongs to the programs using finite-difference methods, therefore finite-resolution effects have to be taken into account. The computational *grid resolution* is given in pixels per lattice unit with a lattice unit being one basis vector in a given direction. Apart from the above-mentioned computational grid, there is a mesh at each grid point. The dielectric constant is averaged over this mesh of points so as to obtain an effective dielectric constant. An increase in the *mesh size* renders the average dielectric constant more sensitive to small structural variations, even without an

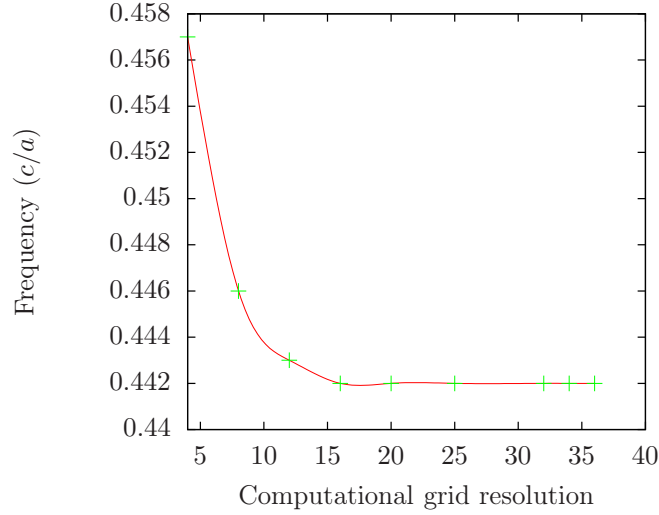


Figure 2.2: Valence band frequency as a function of computational grid resolution. Line as a guide to the eye. Note that the valence band frequency does not change when increasing the computational grid resolution above approximately 16.

increase in the grid size. On the other hand, longer computational time for the dielectric function needs to be taken into account. [10, 13]

We chose the value 16 for the mesh size. The band structure is calculated around the K -point of the Brillouin zone. From the band structure the relative band gap size, sometimes also called *gap-midgap ratio*, is calculated. Letting ω_m be the frequency at the gap middle, the gap-midgap ratio is defined as $\Delta\omega/\omega_m$ and expressed as a percentage. In order to find the necessary resolution, band structure calculations are performed for different values of the resolution. The frequencies of the valence band are plotted as a function of the resolution. The frequency does not change above a resolution of 16; see Figure 2.2. Further calculations were performed using this value.

2.1.2 Results of band structure simulations

Using the finite-difference frequency-domain (FDFD) method implemented in MPB, band structures for Si_3N_4 PC slabs with different air hole radii are simulated. The simulation is performed along the path $\Gamma - M - K - \Gamma$ with 24 k -points interpolated between each pair of consecutive points.

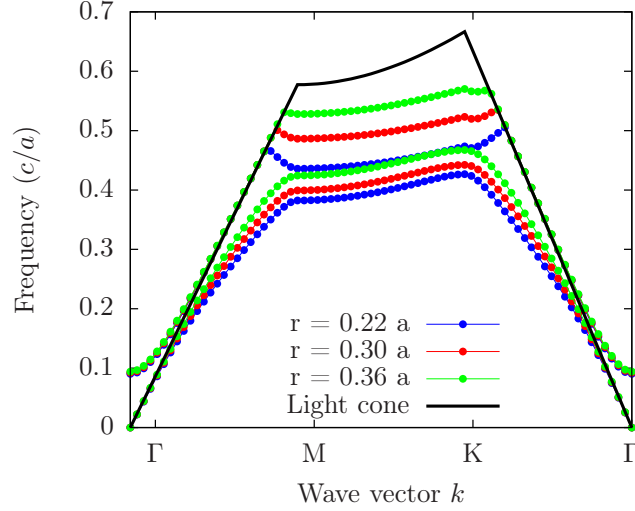


Figure 2.3: Projected band structure of photonic crystal slab with different radii. Thickness $h = 0.7a$ with TE modes. The light cone $\omega = kc$ is plotted in thick black. Note that an increase in r pushes the bands up.

Optimization of the air hole radius

A band gap exists for Si_3N_4 PC slabs with air holes only for TE modes, i.e. \mathbf{H}_z , \mathbf{E}_y and \mathbf{E}_x , [13], see Figure 2.3. Next, the optimization of the air hole radius is discussed. FDFD simulations were performed for a PC slab with a slab thickness of $t = 0.5a$. The hole radius is varied and the resulting band structure is plotted, see Figure 2.4. A hole radius of approximately $r = 0.35a$ maximizes the gap size (ca. 12%). Further increasing or decreasing the radius reduces the band gap size. The effect of radius variation can be further seen in Figure 2.4; increasing the radius increases the band gap size and the frequencies of the bands plotted. This behavior might be explained by means of the variational theorem. According to the variational theorem [13, 40], the electric field \mathbf{E} tends to concentrate in regions of high dielectric constant $\varepsilon(\mathbf{r})$ while being orthogonal to lower frequency modes. This statement explains the band splitting. The first band, i.e. the dielectric band, has most of its energy in the dielectric regions and has a low frequency. In order to be orthogonal to the dielectric band the second band, i.e. the air band, the dielectric band needs to have a nodal plane of higher frequency [13].

Increasing the radius of the air holes leads to growth of the band gap size approximately till $r = 0.36a$. Considering the electric field distribution of the H_z component at $k = M$ [40], shows that increasing r/a forces the electric fields into regions of lower refractive index n thereby increasing the frequency which results in a larger band gap.

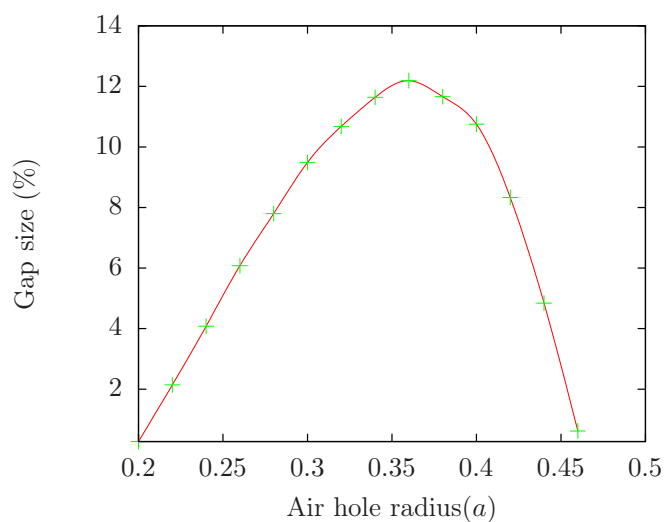


Figure 2.4: Relation between band gap size and air hole radius. Thickness $t = 0.5 a$. Line as guide to the eye. Note that the maximal band gap size is reached for $r = 0.36 a$.

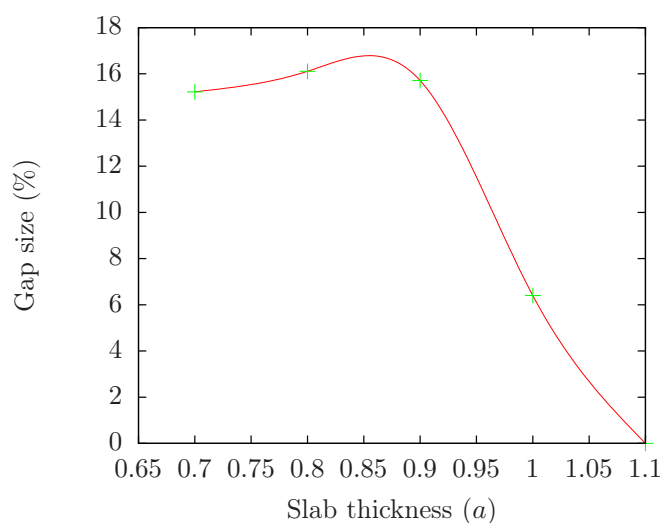


Figure 2.5: Calculated photonic crystal slab band gap size as a function of the slab thickness for $r = 0.35 a$. Line as a guide to the eye. There is no clear maximum, it is probably around $t = 0.85 a$.

Optimization of the slab thickness

After the optimal radius has been found, further simulations have been performed using this value of the radius in order to find the optimal PC thickness. The term thickness refers to the realm of the simulation, in fact the slab-thickness is fixed by the choice of the wafer and the processes used to produce the PC. From Figure 2.5, we can see that the band gap size grows when the thickness of the photonic crystal is increased till

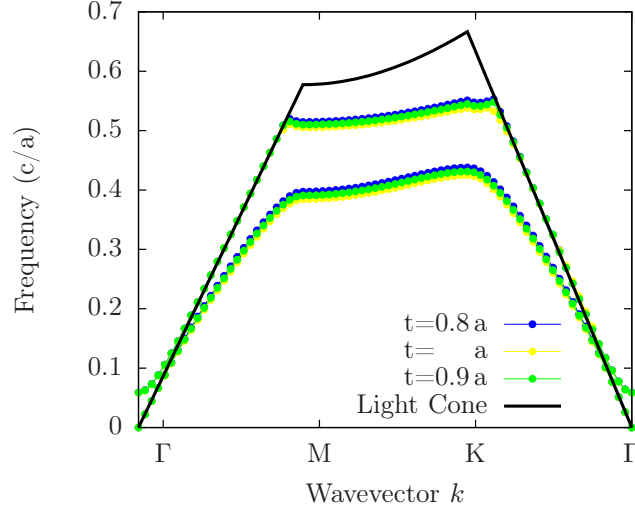


Figure 2.6: Calculated photonic band structure for different PC slab thicknesses. Radius $r = 0.35a$.

a certain point, then it decreases. The ideal thickness of a PC can be obtained when considering the two extreme cases. Is the slab too thin, weak guiding will occur (in the best case). Therefore the band gap, i.e. the normalized frequency difference between the air band, and the dielectric band becomes so small that it will not be considered a gap. A very thick slab, however, will introduce higher-order modes and thus destroy the band gap [39]. According to [39], the optimal slab thickness is calculated as

$$h \approx \frac{1}{2\omega_{\text{gap-bottom}} \sqrt{\langle \epsilon \rangle}}, \quad (2.1)$$

with the frequency given in units of c/a and the thickness in units of a . Plugging in $\bar{\epsilon}_{\text{TE}} = \langle \epsilon \rangle_E \approx \epsilon_{\text{high}}$ [39] yields $h = 0.57a$ which does not compare well with the calculated thickness $h = 0.85a$.

2.2 Finite-difference time-domain simulations

Band gap size and band structures were obtained using MPB, now results from MEEP simulations follow. Mode profiles and quality factor calculations become available through FDTD simulations without being bound by symmetry constraints [10]. *L3* cavities, see Figure 2.7, were simulated. The inner cavity holes were shifted and the air hole radius was changed.

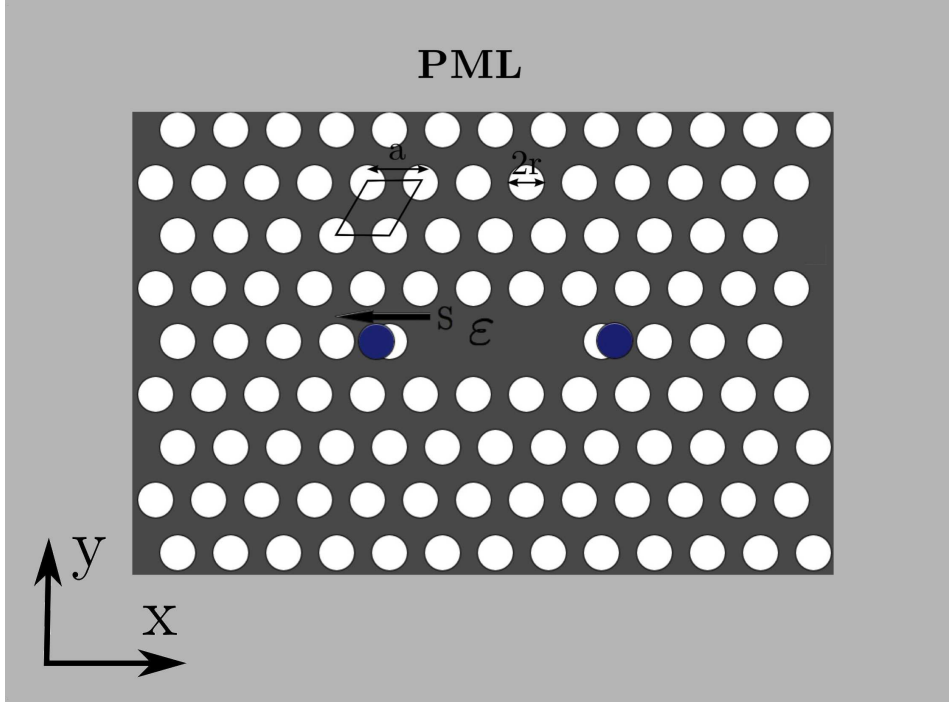


Figure 2.7: Photonic crystal $L3$ cavity with coupler and PML. The design follows [43]. The air hole radius r , the inner cavity air hole (blue) displacement s and lattice constant a can be changed.

One restriction has been added: ideally the resonance wavelength of the fundamental cavity mode should be around $\lambda = 637 \text{ nm}$, the resonance of the NV center electron transition between the ground 3A and excited 3E states [41], see Sec. 1.2.

We are only interested in the fundamental mode, see Figure 2.8. This mode has the largest quality factor and a small modal volume V in the order of ≈ 1 and is therefore interesting [42].

2.2.1 Optimization and investigation of $L3$ cavities

So far, we focused on ideal PCs, i.e. PCs without defects. We now turn to the case where a defect is introduced, the symmetry is therefore broken. As periodic boundary conditions are not applicable here, the question of the system size becomes acute. The $L3$ cavity, see Figure 2.7, is simulated for different PC sizes. The air hole radius size r , the slab-thickness t , the lattice constant a as well as the displacement of the inner cavity air holes s have been varied. It has been decided not to implement additional modifications to increase the quality factor Q further as they complicate the fabrication

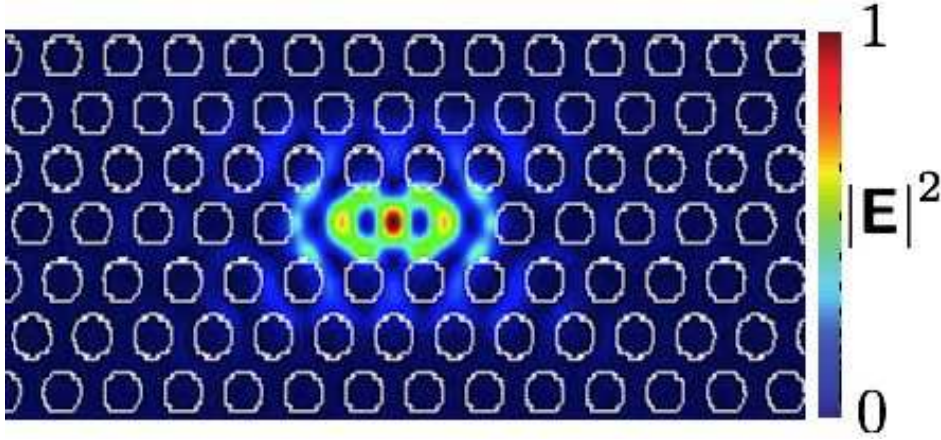


Figure 2.8: Calculated $|\mathbf{E}|^2$ intensity pattern for $L3$ defect with displacement of inner $L3$ cavity holes $s = 0$. See also schematic Figure 2.7. Thickness $t = 0.82a$, air hole radius $r = 0.3a$. Fundamental mode obtained from simulation. Note the vanishing electric field intensity in the air holes next to the cavity—a sign for the localization of the E-field.

process. Possible improvements not realized include an additional change of the radius r' of the shifted inner cavity air holes and decreasing the radius r'' of the other inner holes forming the cavity [44].

Finite size effects

The PC has a size N columns by M rows. The number of rows M and the number of columns N are varied, the ratio $M/N \approx 0.7$ is constant.¹ Apparently, see Figure 2.9, once a certain size (here $M = 21$) is reached the quality factor does not change. This behavior is no surprise; it agrees in fact with the decomposition of the quality factor Q into two contributions, Q_{\parallel} and Q_{\perp} . While the in-plane component Q_{\parallel} is basically a function of the number of rows/columns [13, 25], i.e. of hole layers, it is the out-of-plane component Q_{\perp} that dominates Q . Apart from the size of the system, the simulation time has to be chosen wisely. Small spectral width comes in the frequency domain at the cost of longer computational time. Of course, in this case finite-difference frequency-domain methods would be more efficient and many simulations that can be implemented in MEEP could be also simulated using MPB.

¹This choice is not arbitrary, approximately this figure was found in many papers.

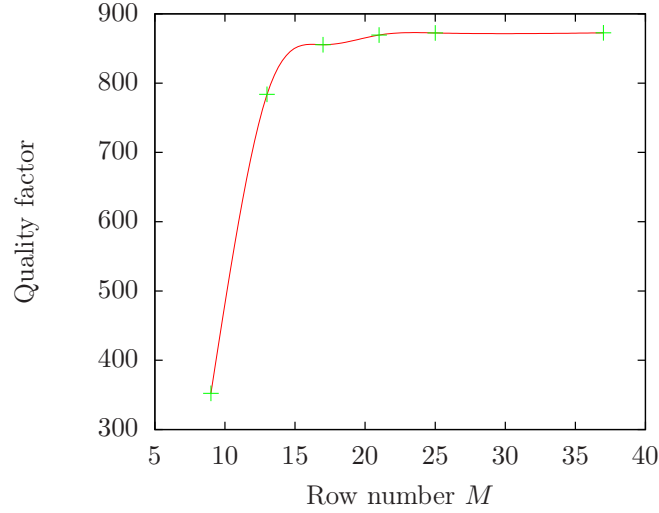


Figure 2.9: Quality factor of fundamental mode of photonic crystal cavity as a function of row number M . Thickness $t = 0.875$, radius $r = 0.26$. Line as guide to the eye. Note that increasing M above $M = 21$ does not change the quality factor.

Modifications of the geometry of a $L3$ cavity

Now having found the minimal size of the PC required to obtain reasonable values of the quality factor, the next step is to change the air hole radius to improve the quality factor. Additionally, the inner holes of the $L3$ cavity will be displaced. Further optimization will aim at reducing out-of-plane losses. This is achieved by reducing the coupling to free-space modes [13, 25, 27].

Optimization of air hole radius and inner hole displacement

It follows from the simulations, see Figure 2.10, that reduction of the air hole radius entails an increase in Q . The range for the air hole radii is limited by the finite radius size that can be experimentally realized. An upper boundary is given by the necessary air hole separation. At least to a certain extent an increase in the quality factor can be seen by comparing the spatial \mathbf{E} field intensity of optimized (regarding Q) and unoptimized PC cavities. In the case of unoptimized cavities, the \mathbf{E} field will be found also in the air holes, as opposed to the optimized cavities that do not exhibit this behavior. It would seem then that decreasing the hole size leads to a smoother, more Gaussian intensity profile of the electric field, a typical feature of high Q .

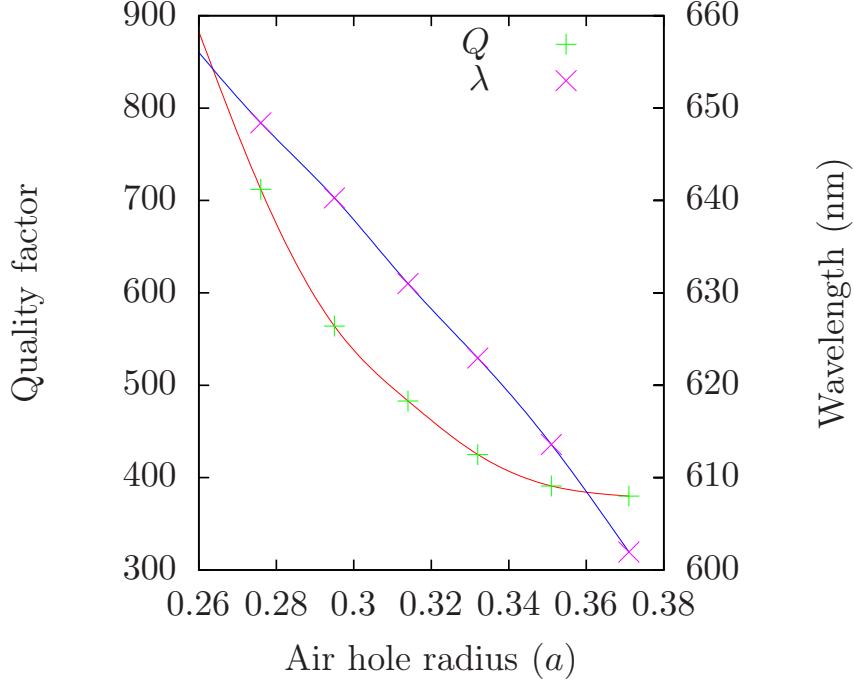


Figure 2.10: Calculated quality factor Q and resonance wavelength λ as a function of air hole radius. Line as guide to the eye. The lattice constant is $a = 263$ nm corresponding to a slab-thickness of $t = 0.82 a$.

As demonstrated in prior research [21], a significant improvement of the quality factor Q can be achieved by displacement of the inner cavity holes, see Figure 2.11. The displacement s leads to a minor change in the resonance peak frequency. Large displacements s may introduce new modes though improving the quality factor. Furthermore, complications concerning the fabrication may arise from such displacements.

Variation of slab-thickness

The slab-thickness has a significant influence on the band gap size as demonstrated above. Furthermore, the slab-thickness has an influence on the quality factor Q and the peak resonance frequency. Changing the thickness moves the photonic bands as can be seen in the band structure Figure 2.6. Increasing the slab thickness pushes higher order modes down; the wavelength is increasing. As can be inferred from Figure 2.12, $t < 0.85 a$ has to be chosen to reach the target wavelength of $\lambda_{N-V} = 637$ nm for the nitrogen vacancy center. Further simulations have shown that the target wavelength can be reached when choosing a slab-thickness of $t = 0.82 a$.

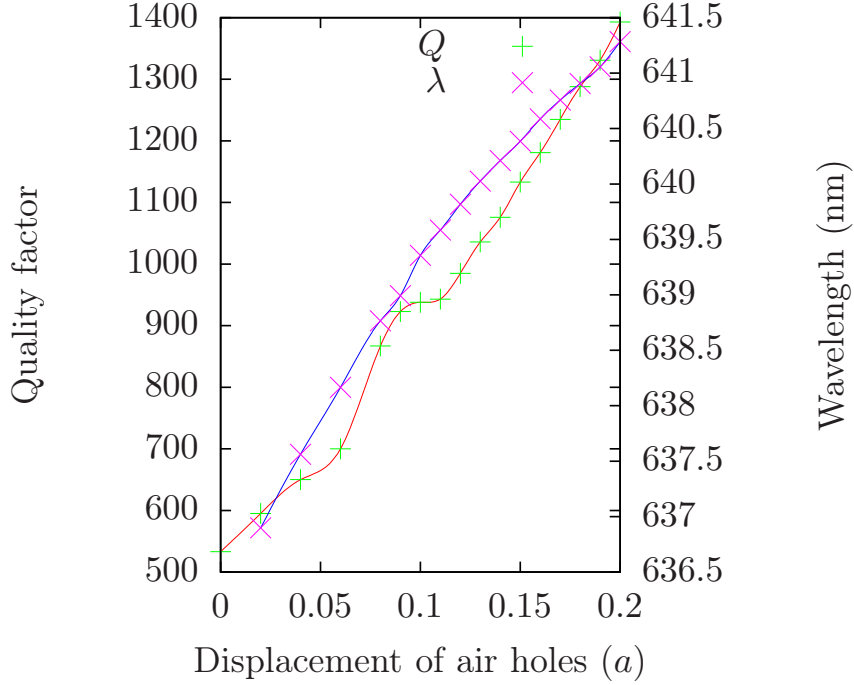


Figure 2.11: Calculated quality factor Q and resonance wavelength λ of PC with displaced inner holes of cavity. Radius $r = 0.3a$ and slab-thickness $t = 0.82a$. Line as guide to the eye.

Coupling efficiency

One of the crucial problems is the coupling of cavities into waveguides. Following [45], the coupling of a photonic crystal linear $L3$ cavity is theoretically investigated, see Figure 2.13. Energy transfer into the waveguide reduces the Q of the coupled cavity. The total Q of a coupled cavity can be decomposed into an inverse sum of the uncoupled cavity quality factor Q_c and the waveguide quality factor Q_{wg} :

$$Q^{-1} = Q_c^{-1} + Q_{wg}^{-1} \quad (2.2)$$

The coupling efficiency $\eta = Q/Q_{wg}$ expressed in percent is the interesting figure of merit. The $L3$ cavity has been coupled to a $W1$ waveguide. More generally, a Wn defect involves the removal of n rows of holes. The number of holes separating between cavity and waveguide has been varied, see Figure 2.14. The best coupling from the PC cavity into the PC waveguide is achieved for a one hole separation, see Table 3.1. For a one hole separation, the symmetry break is the smallest, coupling is therefore better than in the case of two or three holes separation. All realized photonic crystals rely on a

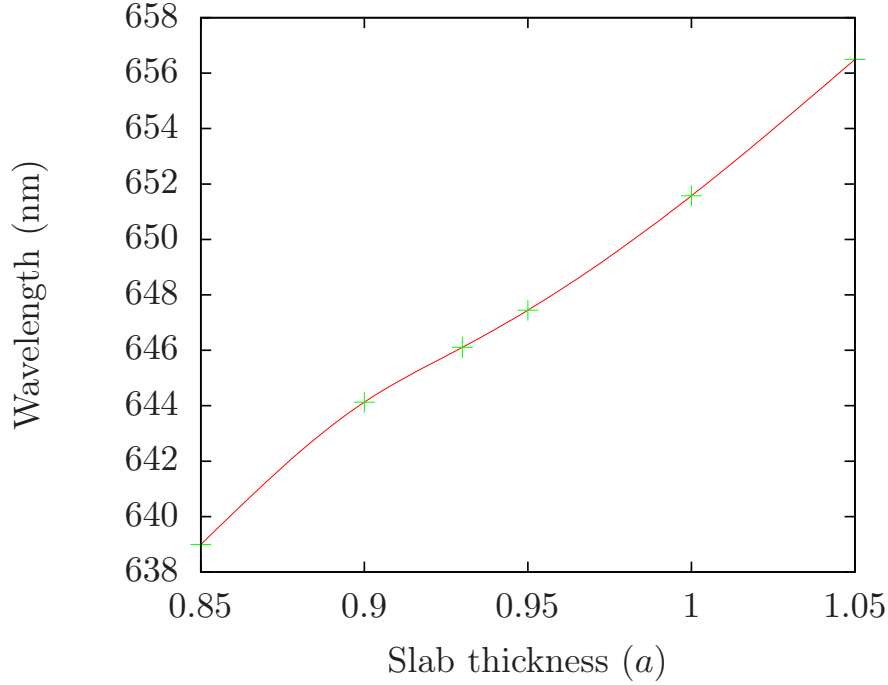


Figure 2.12: Calculated resonance peak wavelength for different slab-thicknesses. Line as guide to the eye. The lattice constant is $a = 263$ nm, air hole radius $r = 0.31a$. Notice the almost linear relation between λ and t .

No. of separating holes	Q	Q_{wg}	Q_{c}	η (%)
1	498	1250	827.79	39.84
2	811	41406	827.2	1.96
3	826	417885	827.64	0.2

Table 2.1: Simulation results for the coupling efficiency from the PC cavity into the PC waveguide. Simulated for 1, 2 and 3 holes separation. The simulated structure is shown in Figure 2.14. The highest coupling efficiency is reached for one hole separation.

one hole separation. For practical applications, much higher coupling efficiencies are required. Tilted waveguides [45] are one way. Optimizing the coupler design, however, was not within the scope of the thesis.

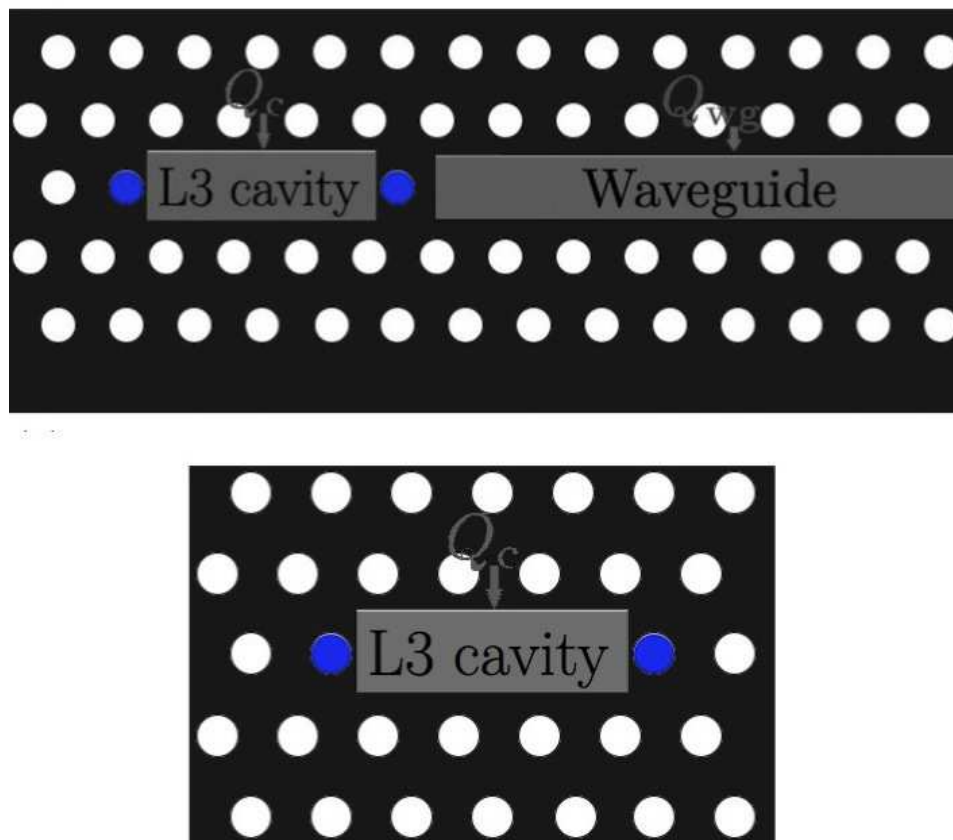
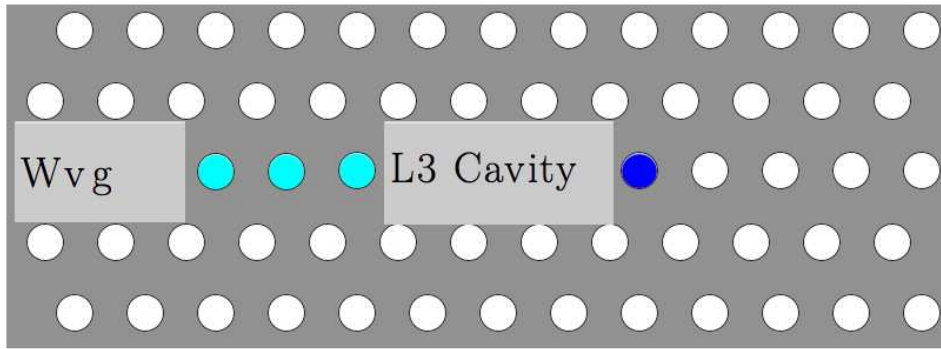
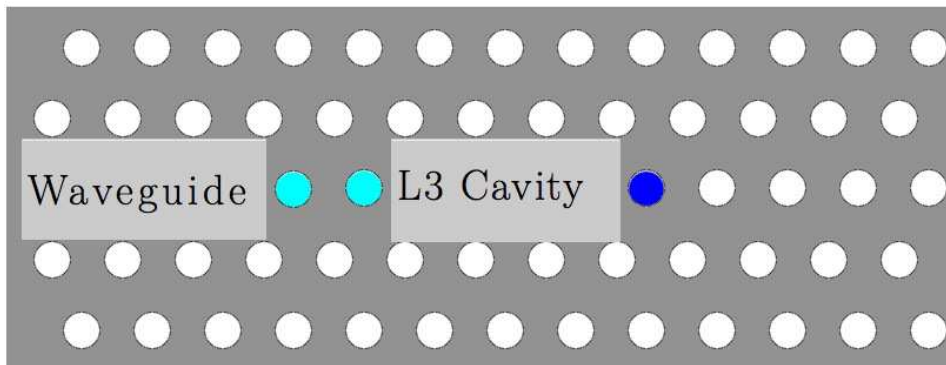


Figure 2.13: Schematic view of the different Q -contributions of the system cavity (Q_c) and waveguide (Q_{wg}). The total Q is given as $Q^{-1} = Q_c^{-1} + Q_{wg}^{-1}$.

(a)



(b)



(c)

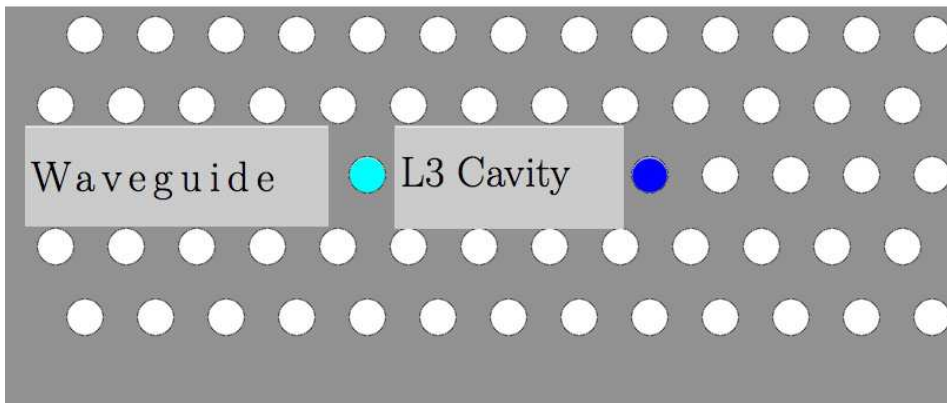


Figure 2.14: Visualization of *L3* cavity coupled into a waveguide. The number of separating holes (cyan) has been varied (3, 2 or 1 holes). The other parameters are identical to Figure 2.7.

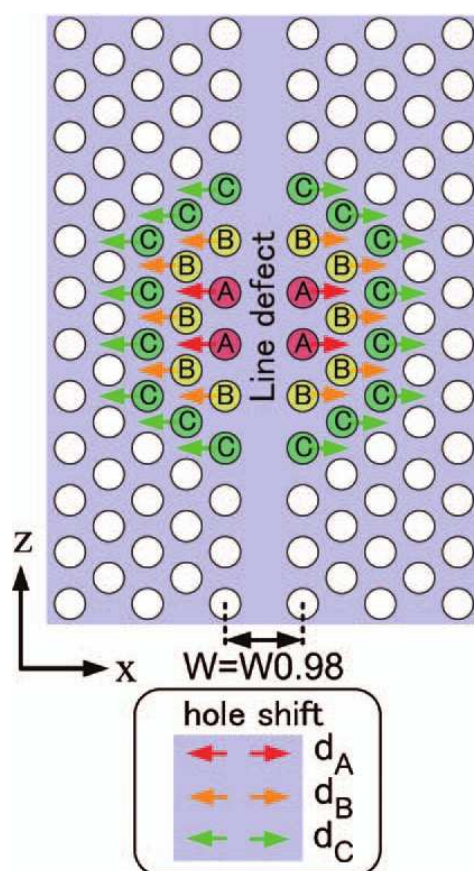


Figure 2.15: Visualization of nanocavity realized by local width modulation of a line defect. Line defect width ($W0.98$, i.e. 0.98% of $W1$ waveguide width). Holes A, B, C are shifted by distances d_A , d_B and d_C , respectively, following the arrow and form a tapered shift structure. $d_A > d_B \geq d_C$. From [46].

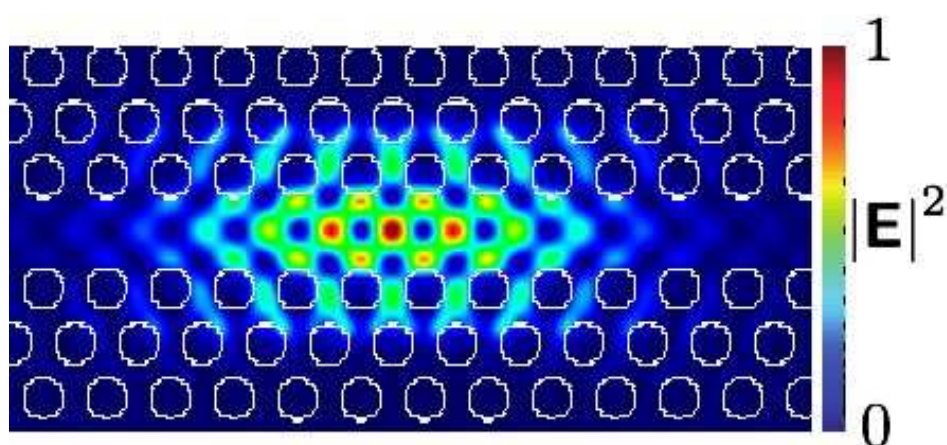


Figure 2.16: Calculated $|\mathbf{E}|^2$ intensity pattern for tapered shift structure, see Figure 2.15. Fundamental mode obtained from simulation. Note the vanishing electric field intensity in the air holes next to the cavity—a sign for the localization of the \mathbf{E} field.

2.2.2 Cavity realized by local width modulation of a line defect

Following [46], the width of a waveguide W is changed. It has been shown [47] that changes of the waveguide width influence mode guiding in the PBG. The researchers showed there that decreasing the waveguide width from 100% to 70% rendered the waveguide single-mode.

Additionally, holes are shifted thereby forming a high- Q nanocavity, see Figure 2.15. It is proposed to use the displacements $d_A > d_B \geq d_C$. In the produced samples hole shifts d_A , d_B , and d_C of x , $2x/3$ and $x/3$ respectively, were realized. The distance between the center of adjacent holes is $a\sqrt{3}$, so the basic line defect $W1$ means $W = a\sqrt{3}$, with a denoting the lattice constant. A value of $x = 0.029a$ corresponding to 7.5 nm has been chosen. A similar value has been chosen by [46]. These values were not changed. High- Q nanocavities with $Q \approx 10^5$ were simulated for $r = 0.26$ and slab-thickness $t = 0.87$. The target wavelength is the $\lambda_{N-V} = 637$ nm so the slab-thickness, i.e. the lattice constant in fabrication and the air hole radius had to be adjusted. The lattice constant is $a = 259$ nm.

For the simulation, the size of the structure was 25×49 air holes. A long simulation time of 2000 MEEP time steps was required to obtain correct values for the high quality factors Q expected. The computational simulation time was increased further by problems when using all symmetry properties inherent in the simulated system. As in the case of $L3$ cavities, the quality factor of the fundamental mode, see Figure 2.16, was simulated as this mode promises the highest Q . The width modulation of the waveguide plays an important role regarding frequency, see Figure 2.18 and even more so regarding the quality factor Q . High Q values up to 700000 have been predicted, see Figure 2.17. The modal volume is around $V \approx 6(\lambda/n)^3$ and therefore larger than in [46], where a high- n material was used. The peak resonance is in the visible spectral region. The only draw-back of the simulations is that air hole diameters of ca. 135 nm would be required. Production of such holes is not possible at the moment at the fabrication facility of the Helmholtz-Zentrum Berlin für Materialien und Energy GmbH (HZB), formerly BESSY and HMI. The fabrication is further complicated by the small displacements of the holes required for the design; the minimal displacement is $d_C = 2.3$ nm.

In this chapter we reported the influence of slab-thickness and air hole radius of hexagonal silicon nitride photonic crystal slabs on band gap size and band structure. Furthermore, the quality factor of $L3$ cavities was optimized by changing the air hole radius and slab-thickness. Simulations of a PC nanocavity realized by local width modulation of a line defect promise high- Q values in the visible spectral range.

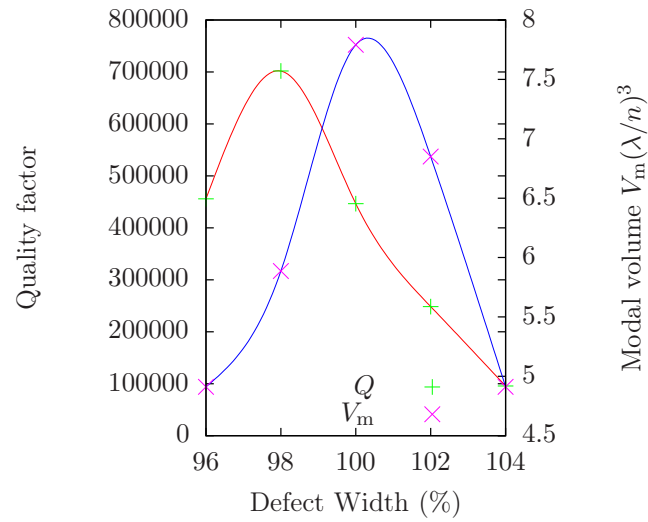


Figure 2.17: Quality factor and modal volume of a line defect with shifted inner holes for different waveguide widths with $r = 0.26a$ and $t = 0.87a$. Line as guide to the eye.

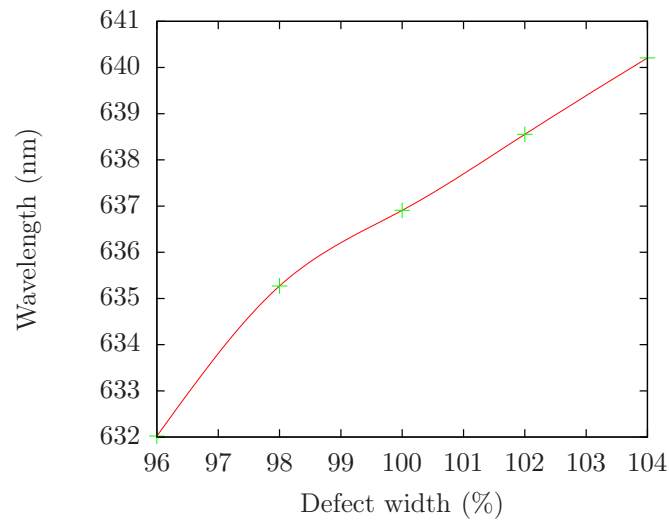


Figure 2.18: Peak resonance frequency of fundamental mode of a line defect with shifted inner holes for different waveguide widths with $r = 0.26a$ and $t = 0.87a$. Line as guide to the eye.

Chapter 3

Fabrication and Characterization

We shall offer a concise overview over the methods used to produce and to characterize the photonic crystal samples in this chapter. Selected results will be presented in this chapter.

3.1 Fabrication of photonic crystal cavities

All samples were produced at the HZB using electron beam lithography and reactive ion etching (RIE) based on stoichiometric silicon nitride (Si_3N_4) [48] with $n \approx 2$ in the visible spectral range. Low-pressure chemical vapor deposition (LPCVD) was used by the producer to grow a thin Si_3N_4 layer on the silicon (Si) to fabricate the Si_3N_4 wafer (Si-Mat, Germany). The Si layer of the wafer had a thickness of $525\text{ }\mu\text{m}$, the thermally oxidized silicon dioxide (SiO_2) sacrificial layer layer a thickness of $2.2\text{ }\mu\text{m}$, and the Si_3N_4 layer a thickness of 230 nm . A tolerance of $\pm 5\%$ has to be added to the above-mentioned thickness values according to the product specification.

For the fabrication procedure, see Figure 3.1, the steps taken will be described briefly, a more detailed description can be found in [49]. The methods used are described in great detail in [1].

Even though photonic crystal samples based on Si_3N_4 have been produced for different theses [25, 29, 40, 49] the documentation was not sufficient. Furthermore, the chemical processes change with time. Thus, the need for new processes arose.

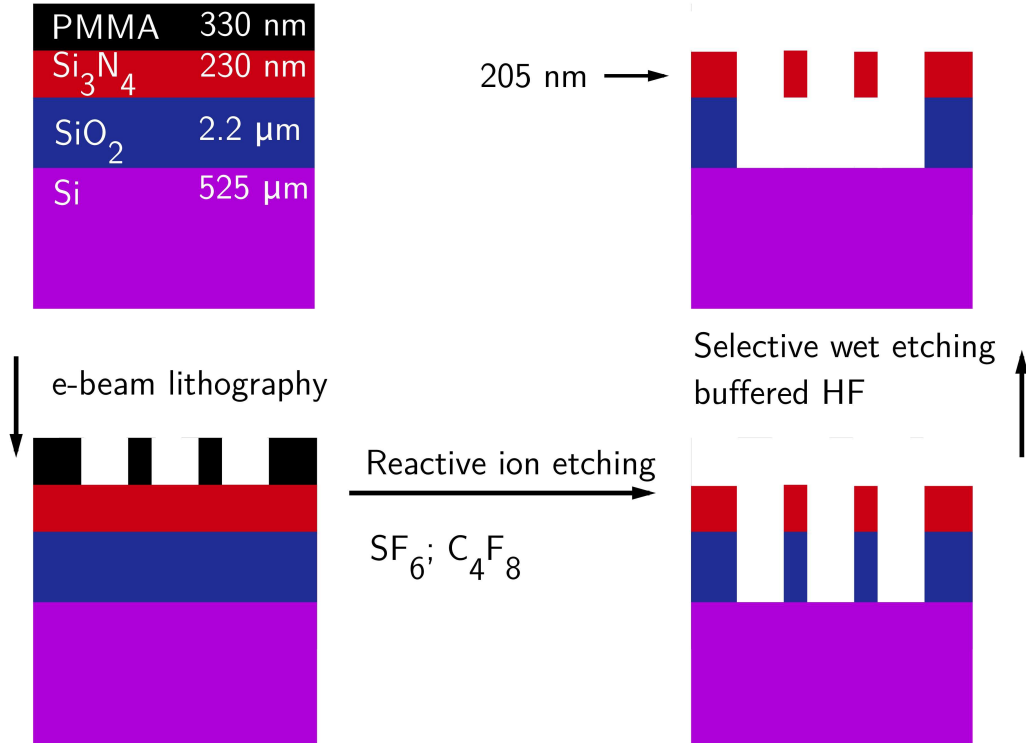


Figure 3.1: Schematic of fabrication process for Si_3N_4 photonic crystals slabs. The individual steps are explained in the main text.

The fabrication process comprises two parts. First a pattern was generated and written in the sample resist. This pattern had to be transferred to the Si_3N_4 layer through etching processes.

3.1.1 Pattern generation

- **Creation of a layout.** A photonic crystal layout had to be created, this was done using the *Gdspy* software toolkit.
- **Spin-coating** for 60 s was used to deposit a 330 nm 2.2 M-polymethylmethacrylate (PMMA, Micro Chem. Corp., USA) layer of *positive resist* on the wafer. The PMMA covered sample was then dried on a hot plate for three minutes at 180° C.
- **Electron beam writing.** The pattern was written by means of a 30 kV LEO 1560 (Zeiss SMT, Germany) scanning electron microscope (SEM) using the Nanomaker© lithography software (Interface Company, Russia). A focused electron beam (electron beam lithography, EBL) scans the resist-covered sample in a specified pattern.

- **Developing.** Afterwards the exposed resist was developed using the developer AR 600 – 56 (Allresist, Germany) for 30s. The development process is stopped by the stopper AR 600 – 60 (Allresist, Germany) which is applied for 10 s. Subsequent rinsing in isopropyl alcohol and deionized water expose the written pattern.

3.1.2 Pattern transfer

Now, the pattern was transferred onto the Si_3N_4 layer.

- **Dry etching.** So as to etch the Si_3N_4 and SiO_2 layers, reactive ion etching (RIE), a dry etching technique has been used, performed in a Plasmalab 80 plus etcher (Oxford Instruments, UK). A high frequency electrical field establishes a plasma consisting of the reactive gases octafluor cyclobutane (C_4F_8) and sulphur hexafluoride (SF_6). The reactive gas ions react with the substrate surface and it volatilizes. Etching is almost fully anisotropic, so there is little lateral etching. Reactive gas composition, pressure and flow as well as power density of the plasma are important and sensitive parameters. Indeed, a lot of trial and error was necessary till the sample displayed round holes. The RIE took 9 : 30 min to etch the resist layer and to etch the holes through the Si_3N_4 and SiO_2 layers. The layer thicknesses before and after etching were measured using a stylus profilometer. The RIE etch rates in Si_3N_4 differ considerably for large and for small structures. In the latter case they are reduced owing to the capillary effect (this plays a role especially for the air holes). The etch rates (RIE) for the different substrates were calculated from the substrate thicknesses before and after etching a certain time. The etch rate for larger structure is approximately 32 nm/s, for smaller structures approximately 24 nm/s.
- **Wet etching.** In the last step, the sacrificial SiO_2 layer below the Si_3N_4 layer is dissolved. Selective wet etching relied on a 5% mixture of hydrofluoric acid (buffered HF) and H_2O with HF: H_2O (1:1) in ammonium fluoride (NH_4F). As opposed to dry etching, wet etching is isotropic, i.e. the etching rate is the same in depth and lateral [1]. This is the last step of the fabrication, the final samples can be seen in Figure 3.2. The Si_3N_4 layer thickness has been inferred from scanning electron microscopy (SEM) images, see Figure 3.1, but further research is required to investigate the reliability of the values. The minimal air hole radius realized was 150 nm as inferred from the SEM images, see Figure 3.1.

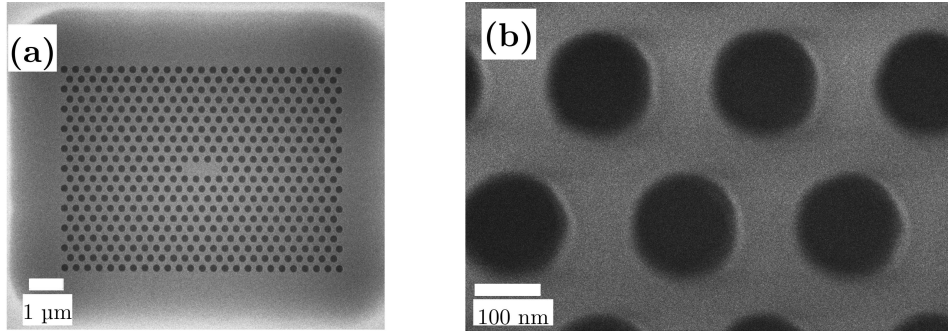


Figure 3.2: Scanning electron images of fabricated *L3* photonic crystal membrane structure. (a) Top view showing cavity and suspension. (b) Close-up view of membrane holes.

3.2 Characterization of photonic crystals

The photonic crystal samples were characterized under ambient conditions at room temperature by means of confocal microscopy. The excitation was realized by a continuous wave (CW) laser (emission wavelength $\lambda = 532$ nm), relying on intrinsic luminescence of the Si_3N_4 itself [48]. A $100\times/0.9$ NA microscope objective has been used to focus the laser beam onto the PC sample and to collect the fluorescence emission excited by the laser. The fluorescence signal and the laser excitation light are separated by means of a beam splitter. In order to maneuver on the sample the fluorescence light is detected by the CCD camera (ORCA, Hamamatsu, Japan). To record a spectrum, the light passes through the spectrograph, the integration time was 30 s. A scheme of the setup is shown in Figure 3.3. Similar methods have been used, for instance, by [25], see there for a more detailed description.

3.3 Experimental results

Additionally to the simulated photonic crystal structures, two types of couplers were produced [43, 50], however no specific experiments were conducted.

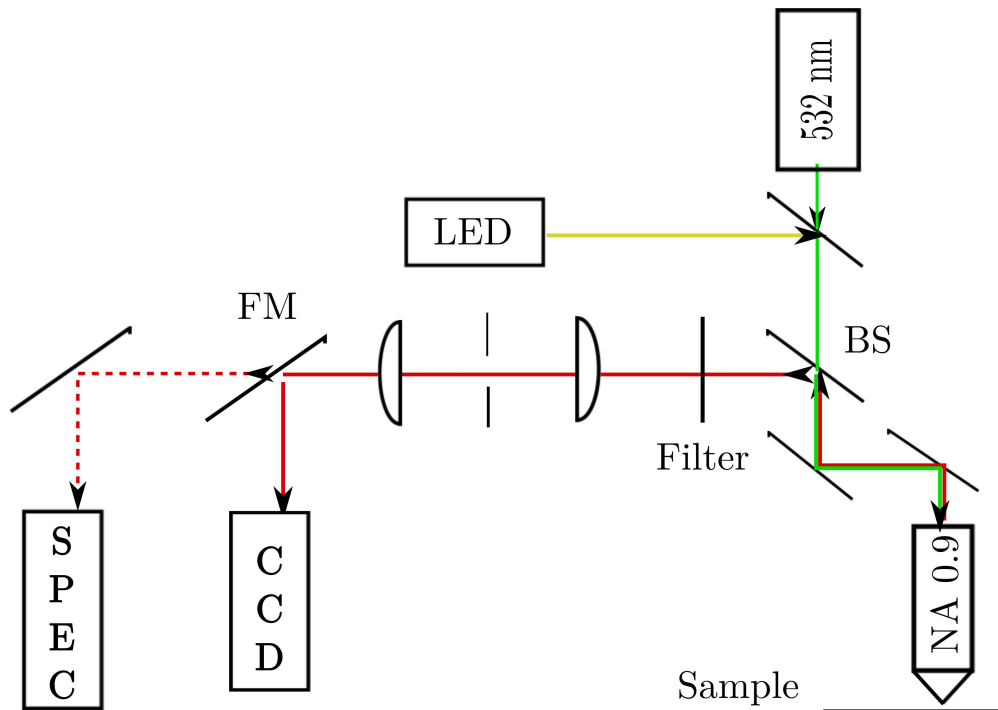


Figure 3.3: Simplified schematic illustration of experimental setup used for the optical characterization of the photonic crystal samples. The following abbreviations have been used: BS – beam splitter, CCD – charge-coupled device, FM – flip mirror, LED – light emitting diode, NA – numerical aperture, SPEC – spectrograph.

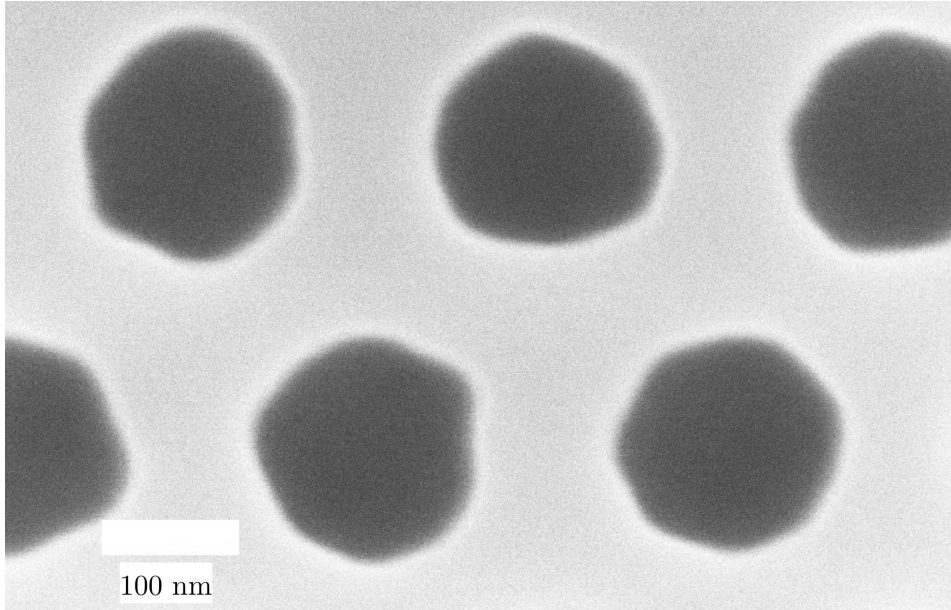


Figure 3.4: Scanning electron microscope image showing air holes of the first produced photonic crystal sample after HF etching. Note the distorted holes.

3.3.1 Fabrication

L3 cavities

The first fabricated samples could not be used. Even before samples could be produced, the proper PMMA thickness had to be found, the proper electron dose had to be simulated and tested. These and other questions could be answered only by trial and error. They are mostly outside the scope of this thesis. Four samples were produced and there was an obvious progress in the quality of the samples.

The first sample, see Figure 3.4, could not be used. The holes with diameter smaller 150 nm were very distorted and too large. Some photonic crystal structures were not etched by HF, even after many hours exposure. Below 150 nm, HF is not very effective. Smaller hole diameters slow down the etching process as the transport of the etched material will take longer. Therefore, the resist layer, that is also etched, albeit with a smaller rate, needs to be thicker. An upper bound for the resist thickness is given by the maximal aspect ratio¹. Increasing the hole diameter solved the problems, see Figure 3.2.

¹The aspect ratio is defined as ratio of width to height of a given structure.

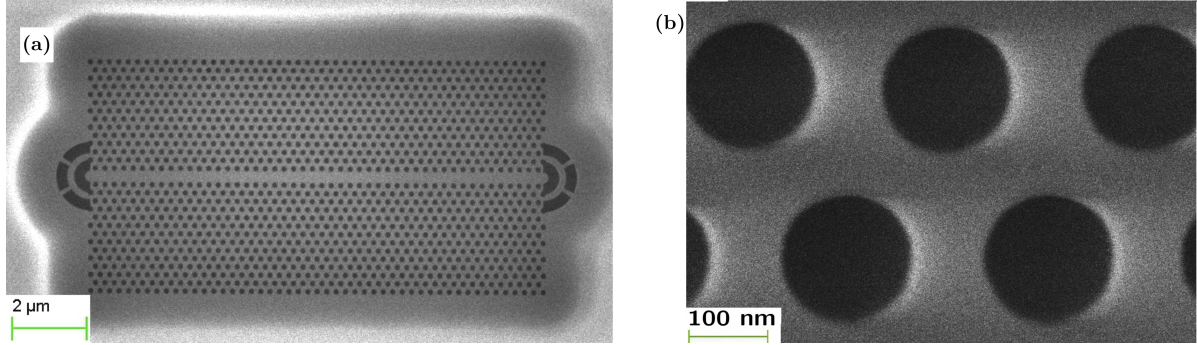


Figure 3.5: Scanning electron microscopy image of a nanocavity realized by local width modulation of a line defect, cf. Figure 2.15. (a) Top view of nanocavity. (b) Close-up view of holes.

Local width modulation of a line defect

Following the proposal reported in [46], the described photonic crystal nanocavities have been realized. Unfortunately time constraints prevented an optical characterization of the PC properties. So, the samples were produced, see Figure 3.5. First fluorescence spectroscopy experiments have been conducted, but no spectrum was detected. From the above-mentioned SEM images, no problems in the production can be inferred.

3.3.2 Measurements

The influence of the radius on Q

The optical properties of the produced samples were investigated using fluorescence spectroscopy relying on the intrinsic luminescence of the Si_3N_4 layer [25, 48]. The quality factors Q of the resonance peaks were obtained using a Lorentzian fit, see Figure 3.6, averaging over ten values. The error bars correspond to the respective standard deviations.

The quality factors for different radii were then plotted, see Figure 3.8. Furthermore the resonance peak wavelength was plotted as a function of the air hole radius, see Figure 3.9. The experimental Q values are smaller than the simulated ideal values. The total quality factor Q of a photonic crystal cavity can be decomposed into two contributions, viz Q_{ideal} of the idealized and therefore perfect simulated structure, and Q_{loss} taking into account losses caused by fabrication imperfections etc. It can be derived [25] that $1/Q_{\text{loss}} = 1/Q - 1/Q_{\text{ideal}}$. Indeed, Q_{loss} does not change very much, see Tab. 3.1.

$\frac{r}{a}$	Q_{loss}
0.31	138
0.33	186
0.35	210
0.37	211

Table 3.1: Difference Q_{loss} between ideal theoretical quality factor Q_{ideal} and experimental quality factor Q for different radii r/a . Note that increasing r/a increase Q_{loss} .

It cannot be assumed here that the value of Q_{loss} is independent of the chosen parameters, namely t , r , s , as it has been shown in the beginning of this section that small r complicates the production. The final Si_3N_4 layer thickness was inferred from the SEM images. This method, however, is not very precise. Apart from this, surface roughness might play a role reducing the quality factor [51] as may the conicity of the air holes [52].

Interestingly, however, there is a difference of approximately 10 nm between the simulated and the experimental peak resonance wavelength. Deviation from the ideal hole geometry as well as the other above-mentioned reasons might also change the peak resonance wavelength, but they cannot account for such great a deviation. The exact radius is not known, the quality factor, however, is very sensitive to the radius, see Figure 2.4. Additionally, the Si_3N_4 layer thickness is subject to uncertainties. Thus, it seems that this two uncertainties might be the reasons for the difference between experiment and simulation. Further research to find the Si_3N_4 layer thickness is in process. No error bars have been plotted for the peak resonance wavelength as the standard deviations of the wavelengths were negligible.

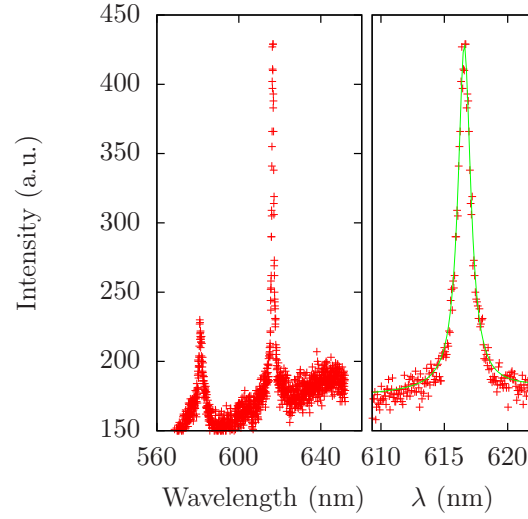


Figure 3.6: Fluorescence spectrum from an $L3$ cavity. The lattice parameters are $a = 263$ nm, $t = 0.82a$, $r = 0.3a$ and $s = 0$. Two resonance peaks (616.57 nm and 580 nm) are shown with Lorentzian fit.

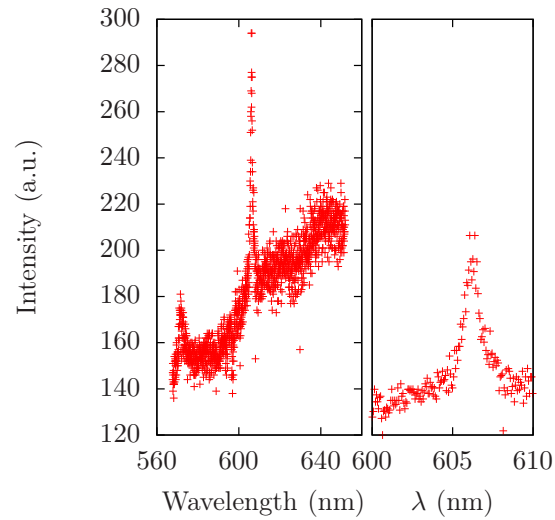


Figure 3.7: Fluorescence spectrum from an $L3$ cavity. The lattice parameters are $a = 263$ nm, $t = 0.82a$, $r = 0.32a$ and $s = 0$. Two resonance peaks at 567 nm and 606 nm are shown. Note the shifted peak wavelengths compared to Figure 3.6.

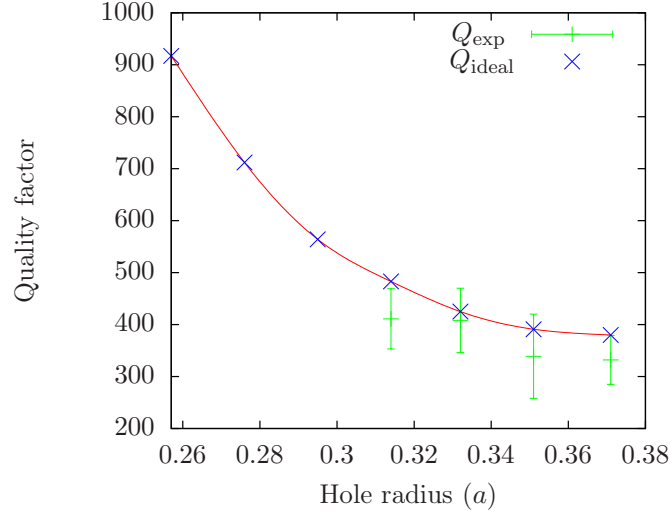


Figure 3.8: Comparison of calculated and experimentally obtained quality factors Q of $L3$ cavities. Experimental values are shown as points. Values from the simulation are plotted as a trend curve. Ten measurements were performed for every r , the errorbars correspond to the respective standard deviation.

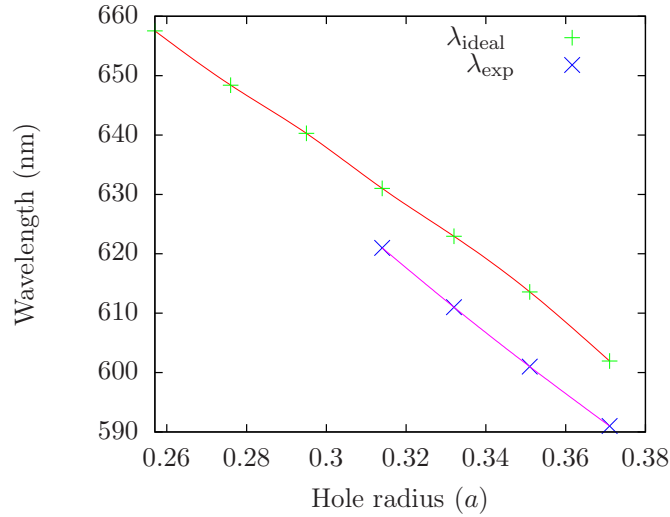


Figure 3.9: Comparison of calculated and experimentally obtained peak resonance wavelengths of $L3$ cavities. A trend curve is plotted for the simulation. The experimental values are plotted as point with a linear fit. The lattice constant has a values of $a = 263$ nm, $s = 0$. Note the shift between experimental and theoretical results along the ordinate.

Chapter 4

Summary and Outlook

4.1 Summary

This thesis introduced basic properties and characteristics of photonic crystals, including the band gap formation, the band structure and the scale invariance. In order to provide a reliable—and possibly a future large-scale fabrication, two-dimensional membrane photonic crystals shall be utilized. Here, we concentrated on simulation and fabrication issues of these structures.

4.1.1 Simulations

Simulations using MPB were conducted to get an overview over the band structure of Si_3N_4 without defects and to get an understanding of the physics behind the band gap. Subsequent MEEP simulations were required to design and produce photonic crystal structures. As far as the spectral range was concerned, the visible wavelength region was chosen. The latter simulations were used to optimize Q of $L3$ cavities with shifted inner holes. It comes out that no high Q is possible with this configuration in the visible spectral range with the inner hole displacement s , air hole radius r and lattice constant a being the only variables. Hence, another structure, a nanocavity realized by local width modulation of a line defect was simulated. Here, indeed high Q could be reached. A layout was then created so that the structures could be produced.

4.1.2 Fabrication and characterization

All the samples were fabricated at the HZB. The first steps involved finding the right parameters for developing the photonic crystals. They were found experimentally. Afterwards the samples were fabricated using standard electron beam lithography. Throughout the fabrication process, different optimizations were introduced so that precise production of photonic crystals with hole sizes down to 150 nm is possible. The samples were characterized by means of confocal microscopy. It was found that the ideal simulated quality factors are smaller than the experimental values by $Q_{\text{loss}} = 200$. For the available Si_3N_4 wafers and the presently implemented fabrication process a further reduction of Q_{loss} seems difficult. Either a better wafer quality or a design which is more forgiving to imperfections will be required.

4.2 Conclusion and outlook

The first two chapters of the thesis offer a glimpse into the fascinating physics of photonic crystals. The simulations showed that there is a wide parameter space to optimize the structures. However, there is no general approach to optimize the two important parameters Q and V_{eff} . Constraints apply regarding the application, e.g. required resonance wavelength, as well as regarding the fabrication process, e.g. available wafer quality and thickness or minimum producible feature size. In addition, more complex features involving efficient waveguide couplers shall be included. It was a goal of this thesis to highlight that in principle the designed structures can be fabricated. A particular interesting simulated structure is the nanocavity realized by local width modulation of a line defect [46].

It promises to be an attractive structure, especially if implemented in the visible spectral range based on Si_3N_4 . It is the high Q of up to 700,000 that renders it the most attractive candidate for different applications in quantum information processing (QIP), quantum electrodynamics (QED) and related fields.

Future studies have to continue systematic experimental investigations of different cavity designs and the limitations imposed by realistic fabrication. This thesis lays the ground at the Helmholtz-Zentrum Berlin for a usually reliable fabrication of Si_3N_4 photonic crystals. The production process is well-documented and will help future generations of photonic crystal researchers.

Acknowledgments

It is time to say thank you. First and foremost, Prof. Oliver Benson has to be mentioned, I am grateful for becoming part of the fascinating NANO research group, dealing with cutting-edge research. Thank you for the advice provided, and the support at every stage of my work. Prof. Andreas Knorr willingly agreed and supported my work in the NANO group at the HU, kudos for the cooperation. I express my deep gratitude to Janik Wolters for his enthusiastic guidance, fresh ideas and constructive criticism—even with his limited time. Carlo Barth’s thesis was the basis for my work. His programming skills and experience in photonic crystal simulations proved to be very helpful. Without him, this work would not be possible. My gratitude also goes to our collaborators Jürgen Probst and Max Schoengen at the Helmholtz-Center Berlin for Materials and Energy GmbH. Notwithstanding their multiple obligations, and plethora of cooperations they were able to redevelop the processes necessary to produce magnificent photonic crystal slabs. I learned that patience is of paramount importance, trial and error; after many trials the right parameters for the fabrication were found. My brother Alexander proof-read my thesis, and marked the mistakes without mercy; thank you so much. Finally, I want to thank my parents for their belief in me and their support in all its different forms. It is to them that my thesis is dedicated.

Bibliography

- [1] Z. CUI. *Micro-Nanofabrication: Technologies and Applications*. Springer, 2006.
- [2] S. KINOSHITA, S YOSHIOKA, and J MIYAZAKI. Physics of structural colors. *Rep. Prog. Phys.*, **71**:7 (2008), 076401.
- [3] M. KOLLE. *Photonic Structures Inspired by Nature*. Springer, 2011.
- [4] S. KINOSHITA, S. YOSHIOKA, and K. KAWAGOE. Mechanisms of structural colour in the Morpho butterfly: cooperation of regularity and irregularity in an iridescent scale. *P. Roy. Soc. Lond. B Bio.*, **269**:1499 (2002), 1417–1421.
- [5] K. BUSCH et al. Periodic nanostructures for photonics. *Phys. Rep.*, **444**:3-6 (2007), 101–202.
- [6] LORD RAYLEIGH. On the maintenance of vibrations by forces of double frequency, and on the propagation of waves through a medium endowed with a periodic structure. *Philos. Mag. Series 5*, **24**:147 (1887), 145–159.
- [7] E. YABLONOVITCH. Inhibited spontaneous emission in solid-state physics and electronics. *Phys. Rev. Lett.*, **58**:20 (1987), 2059–2062.
- [8] V. P. BYKOV. Spontaneous Emission in a Periodic Structure. *J. Exp. Theor. Phys.*, **35**:2 (1972), 269–273.
- [9] A. BLANCO et al. Large-scale synthesis of a silicon photonic crystal with a complete three-dimensional bandgap near 1.5 micrometres. *Nature*, **405**:6785 (2000), 437–440.
- [10] A. F. OSKOOI et al. Meep: A flexible free-software package for electromagnetic simulations by the FDTD method. *Comput. Phys. Commun.*, **181**:3 (2010), 687–702.
- [11] S. JOHNSON and J. JOANNOPOULOS. Block-iterative frequency-domain methods for Maxwell’s equations in a planewave basis. *Opt. Express*, **8**:3 (2001), 173–177.
- [12] K. BUSCH, M. KÖNIG, and J. NIEGEMANN. Discontinuous Galerkin methods in nanophotonics. *Laser & Photon. Rev.*, **5**:6 (2011), 773–809.

- [13] J. D. JOANNOPOULOS et al. *Photonic crystals : molding the flow of light*. Princeton University Press, 2008.
- [14] M. SKOROBOGATIY. *Fundamentals of Photonic Crystal Guiding*. Cambridge University Press, 2009.
- [15] N. W. ASHCROFT and N. D. MERMIN. *Solid State Physics*. Brooks Cole, 1976.
- [16] J. MAXWELL. *A Treatise on Electricity and Magnetism*. Clarendon, 1892.
- [17] J. D. JACKSON. *Classical Electrodynamics Third Edition*. Wiley, 1988.
- [18] D. KLEPPNER. Inhibited Spontaneous Emission. *Phys. Rev. Lett.*, **47**:4 (1981), 233–236.
- [19] E. PURCELL. Spontaneous emission probabilities at radio frequencies. *Phys. Rev.*, **68**:11 (1946), 681.
- [20] E. YABLONOVITCH et al. 3-dimensional photonic band structure. *Opt. Quant. Electron.*, **24**:2 (1992), S273–S283.
- [21] Y. AKAHANE, T. ASANO, and B.-S. SONG. High-Q photonic nanocavity in a two-dimensional photonic crystal. *Nature*, **425**:6961 (2003), 944–947.
- [22] D. ENGLUND, I. FUSHMAN, and J. VUCKOVIĆ. General recipe for designing photonic crystal cavities. *Opt. express*, **13**:16 (2005), 5961–5975.
- [23] T. YOSHIE et al. Vacuum Rabi splitting with a single quantum dot in a photonic crystal nanocavity. *Nature*, **432**:7014 (2004), 200–203.
- [24] J. BRAVO-ABAD et al. Enhanced nonlinear optics in photonic-crystal microcavities. *Opt. Express*, **15**:24 (2007), 16161–16176.
- [25] M. BARTH. *Hybrid nanophotonic elements and sensing devices based on photonic crystal structures*. PhD thesis. Humboldt-Universität zu Berlin, 2010.
- [26] K. J. VAHALA. Optical microcavities. *Nature*, **424**:6950 (2003), 839–846.
- [27] K. SRINIVASAN and O. PAINTER. Momentum space design of high-Q photonic crystal optical cavities. *Opt. Express*, **10**:15 (2002), 670–684.
- [28] F. JELEZKO and J. WRACHTRUP. Single defect centres in diamond: A review. *Phys. Status Solidi A*, **203**:13 (2006), 3207–3225.
- [29] N. C. NÜSSE. *Hybridstrukturen aus Nanodiamanten, nanoplasmonischen Elementen und photonischen Kristallen*. PhD thesis. Technische Universität Berlin, 2011.
- [30] U. S. INAN and R. A. MARSHALL. *Numerical Electromagnetics: The FDTD Method*. Cambridge University Press, 2011.

- [31] K. YEE. Numerical solution of initial boundary value problems involving maxwell's equations in isotropic media. *IEEE T. Antenn. Propag.*, **14**:3 (1966), 302–307.
- [32] J.-P. BERENGER. A perfectly matched layer for the absorption of electromagnetic waves. *J. Comput. Phys.*, **114**:2 (1994), 185 –200.
- [33] O. HESS. Finite-Difference Time-Domain simulations of photonic crystal defect structures. *Phys. Status Solidi A*, **197**:3 (2003), 605–619.
- [34] A. FARJADPOUR et al. Improving accuracy by subpixel smoothing in FDTD. *Opt. Lett.*, **31**:20 (2006), 2972–2974.
- [35] A. F. OSKOOI, C. KOTTKE, and S. G. JOHNSON. Accurate finite-difference time-domain simulation of anisotropic media by subpixel smoothing. *Opt. Lett.*, **34**:18 (2009), 2778–2780.
- [36] V. A. MANDELSHTAM and H. S. TAYLOR. Erratum: “Harmonic inversion of time signals and its applications” [J. Chem. Phys. 107, 6756 (1997)]. *J. Chem. Phys.*, **109**:10 (1998), 4128.
- [37] V. A. MANDELSHTAM and H. S. TAYLOR. Harmonic inversion of time signals and its applications. *J. Chem. Phys.*, **107**:17 (1997), 6756–6769.
- [38] F. PISANELLO et al. Silicon nitride PhC nanocavities as versatile platform for visible spectral range devices. *Phot. Nano. Fund. Appl.*, **10**:3 (2012), 319 –324.
- [39] S. JOHNSON et al. Guided modes in photonic crystal slabs. *Phys. Rev. B*, **60**:8 (1999), 5751–5758.
- [40] J. STINGL. *Theoretische und experimentelle Untersuchung der Kopplung von Emittern und Mikroresonatoren in photonischen Kristallen*. Diploma thesis. Humboldt-Universität zu Berlin. 2008.
- [41] G. DAVIES and M. F. HAMER. Optical Studies of the 1.945 eV Vibronic Band in Diamond. *P. Roy. Soc. Lond. A Mat.*, **348**:1653 (1976), 285–298.
- [42] A. R. CHALCRAFT et al. Mode structure of the L3 photonic crystal cavity. *Appl. Phys. Lett.*, **90**:24 (2007), 241117.
- [43] C. BARTH. *Design und Optimierung von Wellenleitern und Gitterkopplern für Photonische Kristall-Strukturen*. Bachelor's thesis. Humboldt-Universität zu Berlin. 2011.
- [44] E. KURAMOCHI et al. Ultrahigh-Q two-dimensional photonic crystal slab nanocavities in very thin barriers. *Appl. Phys. Lett.*, **93**:11 (2008), 111112.

-
- [45] A. FARAON et al. Efficient photonic crystal cavity-waveguide couplers. *Appl. Phys. Lett.*, **90**:7 (2007), 073102.
 - [46] E. KURAMOCHI et al. Ultrahigh-Q photonic crystal nanocavities realized by the local width modulation of a line defect. *Appl. Phys. Lett.*, **88**:4 (2006), 041112.
 - [47] M. NOTOMI et al. Structural tuning of guiding modes of line-defect waveguides of silicon-on-insulator photonic crystal slabs. *IEEE J. Quantum. Elect.*, **38**:7 (2002), 736–742.
 - [48] S. V. DESHPANDE et al. Optical properties of silicon nitride films deposited by hot filament chemical vapor deposition. *J. Appl. Phys.*, **77**:12 (1995), 6534–6541.
 - [49] J. KOUBA. *Investigation of silicon nitride based two-dimensional photonic crystals for the visible spectral range*. PhD thesis. Technische Universität Berlin, 2008.
 - [50] A. FARAON et al. Integrated quantum optical networks based on quantum dots and photonic crystals. *New J. Phys.*, **13**:5 (2011), 055025.
 - [51] F. WEN et al. Two-dimensional photonic crystals with large complete photonic band gaps in both TE and TM polarizations. *Opt. Express*, **16**:16 (2008), 12278–12289.
 - [52] P. STRASSER et al. Sidewall roughness measurement inside photonic crystal holes by atomic force microscopy. *Nanotechnology*, **18**:40 (2007), 405703.

Publications

Talk

M. ADLER, C. BARTH, J. PROBST, M. SCHOENGEN, B. LÖCHEL, J. WOLTERS, and O. BENSON “*Design, fabrication and characterization of high-Q photonic crystal cavities in SiN*”, DPG Spring Meeting, Regensburg 2013.

Poster

C. BARTH, M. ADLER, J. PROBST, M. SCHOENGEN, B. LÖCHEL, J. WOLTERS, and O. BENSON “*Design and optimization and fabrication of photonic crystal structures for single photon applications*”, DPG Spring Meeting, Regensburg 2013.

List of Figures

0.1	Blue Morpho—a natural photonic crystal example.	3
1.1	Construction of Wigner-Seitz cell	10
1.2	Visualization of photonic crystal slab with air holes.	14
1.3	Visualization of Snell’s law.	16
1.4	Projected band structure diagram of Si_3N_4 photonic crystal slab.	17
1.5	Band structure diagram of Si_3N_4 photonic crystal slab with point defect.	19
1.6	Visualization of $W1$ waveguide, and $L3$ cavity.	20
1.7	Schematic of NV center.	23
1.8	Yee cube with \mathbf{E} and \mathbf{H} fields.	27
2.1	Visualization of PC slab with air holes.	32
2.2	Valence band frequency as a function of computational grid resolution.	33
2.3	Projected band structure of photonic crystal slab with different radii.	34
2.4	Diagram showing relation between band gap size and air hole radius.	35
2.5	Calculated band gap size as a function of the slab thickness.	35
2.6	Calculated photonic band structure for different PC slab thicknesses.	36
2.7	Visualization of PC $L3$ cavity with coupler and PML.	37
2.8	Calculated $ \mathbf{E} ^2$ intensity pattern for $L3$ defect.	38

2.9	Quality factor of fundamental mode of photonic crystal cavity as a function of row number M	39
2.10	Calculated quality factor Q as a function of air hole radius.	40
2.11	Calculated Q and resonance wavelength of PC with displaced inner holes of cavity.	41
2.12	Calculated resonance peak wavelength for different slab-thicknesses. . . .	42
2.13	The different Q -contributions of the system cavity (Q_c) and waveguide (Q_{wg}).	43
2.14	Visualization of $L3$ cavity coupled into a waveguide.	44
2.15	Visualization of nanocavity realized by local width modulation of a line defect.	45
2.16	Calculated $ \mathbf{E} ^2$ intensity pattern for tapered shift structure	45
2.17	Q and V_{eff} for cavity realized by width-modulation of line defect, for different widths.	47
2.18	Peak resonance frequency of fundamental mode of a line defect with shifted inner holes for different waveguide widths.	47
3.1	Fabrication process for Si_3N_4 photonic crystals slabs.	50
3.2	SEM image of fabricated $L3$ photonic crystal membrane structure.	52
3.3	Experimental setup used for the optical characterization of the photonic crystal samples.	53
3.4	SEM image showing air holes of first photonic crystal sample after HF etching.	54
3.5	SEM image of nanocavity realized by local width modulation of a line defect.	55
3.6	Fluorescence spectrum from an $L3$ cavity.	57
3.7	Fluorescence spectrum from an $L3$ cavity.	57
3.8	Comparison of calculated and experimentally obtained Q for $L3$ cavities. .	58

3.9 Comparison of calculated and experimentally obtained peak resonance wavelengths of $L3$ cavities.	58
--	----

List of Tables

2.1	Calculated coupling efficiency PC cavity - PC waveguide.	42
3.1	Q_{loss} of $L3$ cavity for different r/a	56